TAMPEREEN TEKNILLINEN YLIOPISTO
TAMPERE UNIVERSITY OF TECHNOLOGY

ROOSA-MARIA SALLINEN

INTEGRATING AN ELECTRICAL ENERGY STORAGE TO A GRID-CONNECTED PHOTOVOLTAIC SYSTEM

Master of Science thesis

Examiner: Assist. Prof. Tuomas Messo
Examiner and topic approved by the
Faculty Council of the Faculty of
Computing and Electrical Engineering
on 15th February 2017

ABSTRACT

ROOSA-MARIA SALLINEN: Integrating an Electrical Energy Storage to a Grid-Connected Photovoltaic System
Tampere University of Technology
Master of Science thesis, 61 pages, 1 Appendix pages
October 2017
Master's Degree Programme in Electrical Engineering
Major: Power Electronics
Examiner: Assist. Prof. Tuomas Messo
Keywords: energy storage, battery, photovoltaic, topology, design, distributed generation, intermittency mitigation

As the penetration level of renewable energy sources, such as photovoltaic (PV) and wind power, becomes more and more prevalent, their unpredictable and intermittent nature increases the probability of a mismatch between the produced power and the demand. The reliability, stability, and power quality of the grid degrade if proper actions to overcome these problems are not taken into account. One solution is to utilize an electrical energy storage (EES), such as a battery.

The purpose of this thesis is to provide an insightful and meaningful comparison between the different power electronic topologies utilized in PV-EES distributed generation (DG) systems. One- and double-stage schemes and ac-interfaced batteries are investigated and compared. The topologies are compared on the basis of part count, component sizing, reliability, efficiency, modularity, and control system complexity. The constraints in each approach are identified. The comparisons are conducted by analyzing the topologies and performing real-time simulations.

Based on the aforementioned analysis, it is shown that the addition of the bidirectional dc-dc converter (double-stage inverter) is necessary if the battery terminal voltage is lower than that required for the direct (single-stage) inverter connection. The same applies to the PV modules. Furthermore, the double-stage topology allows more flexibility in the dc-link voltage selection. Thus, the employed control techniques can operate the inverter in a more effective way leading to lower total harmonic distortion (THD) as well as a reduction in the hardware requirements (e.g. filter size). Also, due to the cascaded control scheme of the inverter, faster regulation of the PV voltage can be implemented in the double-stage scheme. However, the single-stage inverter is more efficient owing to the less power conversion stages involved. As demonstrated by simulations with real irradiance data, the battery can be used for intermittency mitigation to compensate the fluctuations in the PV power (power balance), thus providing constant power to the grid.

TIIVISTELMÄ

ROOSA-MARIA SALLINEN: Sähköisen energiavaraston liittäminen verkkoon kytkettyyn aurinkosähkövaihtosuuntaajaan
Tampereen teknillinen yliopisto
Diplomityö, 61 sivua, 1 liitesivua
Lokakuu 2017
Sähkötekniikan koulutusohjelma
Pääaine: Tehoelektroniikka
Tarkastajat: Assist. Prof Tuomas Messo
Avainsanat: energiavarasto, akku, aurinkokenno, topologia, suunnittelu, hajautettu tuotanto

Uusiutuvien energialähteiden, kuten aurinko- ja tuulivoiman, tuotantoon liittyvä epäsäännöllisyys aiheuttaa ongelmia verkon tuotannon ja kulutuksen tasapainottamisessa. Mitä suurempi osa verkkoon syötettävästä tehosta saadaan näistä energiamuodoista, sitä enemmän energian tuotannon ennustettavuus heikkenee, ellei keinoja tasoittaa tuotantoa ole otettu huomioon. Yksi ratkaisu on hyödyntää sähköisiä energiavarastoja, kuten akkuja, hajautetussa sähköntuotannossa.

Tämän diplomityön tavoitteena on vertailla erilaisia topologioita sähköisten energiavarastojen liittämiseksi aurinkosähkögeneraattoriin hajautetun sähköntuotannon hyödyntämiseksi. Vertailluissa topologioissa akku on kytkettynä dc-dc hakkurin kautta joko aurinkopaneelin terminaaleihin tai dc-välipiiriin tai ilman dc-dc hakkuria suoraan vaihtosuuntaajaan. Topologiat asettavat rajoitteita järjestelmän parametreille, säädön toteutukselle, energiatehokkuudelle, modulaarisuudelle ja hinnalle. Vertailu on toteutettu analysoimalla topologioita ja suorittamalla reaaliaika-simulointeja.

Analyysin perusteella akun dc-dc hakkuri on välttämätön erityisesti, jos akun napajännite ei ole tarpeeksi suuri suoraan vaihtosuuntaajaan kytkemisen mahdollistamiseksi. Sama rajoitus koskee aurinkopaneelien dc-dc hakkuria. Lisäksi dc-dc hakkureilla saavutetaan joustavampi dc-välipiirin jännitteen valinta, joka mahdollistaa vaihtosuuntaajan säädön optimoinnin. Tämän ansiosta verkkoon syötetyn virran kokonaisharmoninen särö vähenee ja suotimien kokoa voidaan pienentää. Invertterin säätäessä aurinkopaneelien jännitettä säädön on oltava kaskadisäätö, joten säätö voidaan toteuttaa nopeammaksi hyödyntämällä dc-dc hakkuria. Akun liittäminen suoraan vaihtosuuntaajaan kuitenkin kasvattaa tehonmuuntosuhdetta, sillä dc-dc hakkurin tehohäviöt jäävät pois. Lisäksi työssä simuloitiin todellisen säteilyvoimakkuusdatan avulla akun käyttöä aurinkopaneelien tuottaman tehon heilahtelujen kompensoimisessa.

PREFACE

This Master of Science thesis was done for the Laboratory of Electrical Energy Engineering at Tampere University of Technology (TUT). The examiner of the thesis was Assist. Prof. Tuomas Messo.

I wish to thank Assist. Prof. Messo for his continuous support and encouragement during the whole research process. Special thanks belong to him also for providing me with the access to the laboratory infrastructure at TUT. I would also like to thank everyone who has shown their interest in my thesis—in one way or another—and this way motivated me even further. Moreover, I would like to thank all the graduate students, Ph.D. candidates, and administrative and technical staff who have created a pleasant working environment at the laboratory. Finally, I want to express my sincere gratitude to my family and friends for the support I have had during my entire life.

Tampere, 15.9.2017

Roosa-Maria Sallinen

CONTENTS

LIST OF FIGURES

LIST OF TABLES

LIST OF ABBREVIATIONS AND SYMBOLS

BES	Battery energy storage
BESS	Battery energy storage system
BMS	Battery management system
CC	Constant current
CV	Constant voltage
DG	Distributed generation
EES	Electrical energy storage
ESR	Equivalent series resistance
GaN	Gallium nitride
HIL	Hardware-in-the-loop
IGBT	Insulated Gate Bipolar Transistor
MOSFET	Metal Oxide Semiconductor Field-Effect Transistor
MPP	Maximum power point
MPPT	Maximum power point tracking
P&O	Perturb and observe
PV	Photovoltaic
PVG	Photovoltaic generator
PWM	Pulse width modulation
RHP	Right half-plane of a complex s-plane
SiC	Silicon Carbide
SoC	State-of-charge
SoH	State-of-health
SPWM	Sinusoidal pulse width modulation
THD	Total harmonic distortion
VSI	Voltage source inverter

A	Ideality factor of a PV cell/module
C	Capacitor (subscripts are used for identification)
Δ_{MPPT}	The amplitude of increment and decrement (perturbation) added to the PV voltage reference (or directly to the controller duty ratio) in P&O MPPT algorithm
d	Duty ratio
d_{d}	The d-component of the modulation index
d_{q}	The q-component of the modulation index
f_{g}	Grid frequency
f_{sw}	Switching frequency

i_{in}	The input current of the converter under consideration
i_{L1d}	The d-component of the LCL-type filtered inverter output current
i_{L1q}	The q-component of the LCL-type filtered inverter output current
i_{L2d}	The d-component of the current fed to the grid from the LCL-type filtered inverter
i_{L2q}	The q-component of the current fed to the grid from the LCL-type filtered inverter
i_{o}	The dark saturation current of a PV cell/module
i_{out}	The output current of the converter under consideration
i_{ph}	The light generated current of a PV cell/module
i_{pv}	Current produced by the PV cell/module
k	Boltzmann constant
K	Proportional gain of a controller (subscripts are used for identification)
L	Inductor (subscripts are used for identification)
ω	Frequency of a zero or a pole (subscripts are used for identification)
q	The elementary charge
R_{d}	The combination of the filter-capacitor ESR value and the damping resistor
r_{d}	Diode resistance
r_{s}	Parasitic series resistance
r_{sh}	Shunt resistance
R_{pv}	Static resistance of a PV system
r_{pv}	Dynamic resistance of a PV system
s	Laplace variable
T	Temperature (K)
v_{C}	The voltage across the capacitor
v_{Cfd}	The d-component of the voltage across the capacitor of the LCL-type filter
v_{Cfq}	The q-component of the voltage across the capacitor of the LCL-type filter
v_{in}	The input voltage of the converter under consideration
v_{od}	The grid voltage d-component
v_{oq}	The grid voltage q-component
v_{out}	The output voltage of the converter under consideration
v_{pv}	Voltage across the PV cell/module
v_{t}	Thermal voltage of a PV cell/module
$\boldsymbol{x}$	The state vector of a system in state-space form
$\dot{\boldsymbol{x}}$	The time-derivative of the state vector
$\boldsymbol{u}$	The input vector of a system in state-space form
$\boldsymbol{y}$	The output vector of a system in state-space form

1. INTRODUCTION

Global warming is one of the greatest crises in modern society. The challenges have driven the adoption of renewable energy sources, such as solar and wind power. By utilizing these sources it is possible to provide electricity without damaging natural resources. With a continuous reduction in system cost, these technologies have become one of the main renewable energy sources for the electricity supply.

However, these energy sources tend to be less reliable compared to conventional ones due to their unpredictability and intermittent nature. Their availability has strong daily and seasonal patterns, and the power demand might possess a totally different characteristic than the production has. Fig. 1.1 shows the measured irradiance levels on 3 different days from the solar panels at Tampere University of Technology (TUT). It is clear, that especially on half-cloudy days, the irradiance on the PV panels can experience rapid fluctuation. This behavior also introduces fluctuation to

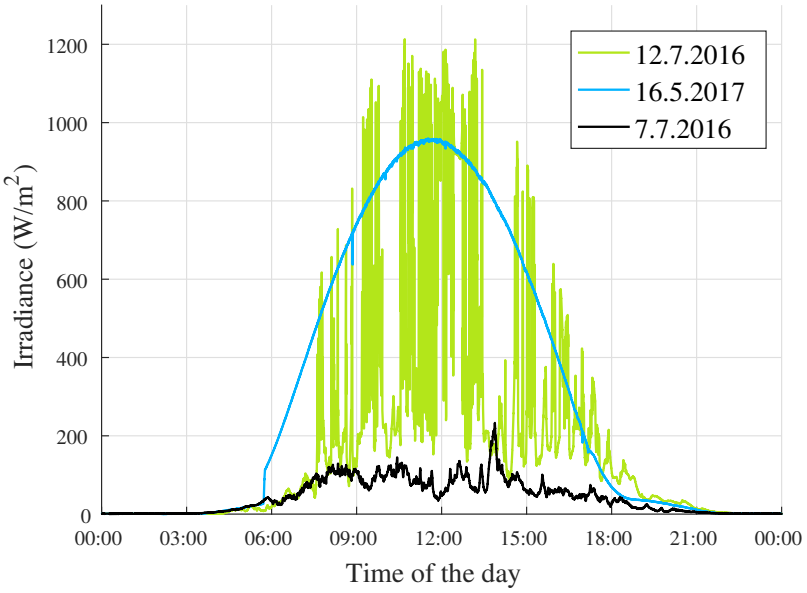

Figure 1.1 *Daily irradiance data measured from the solar panels at the Solar Photovoltaic Power Station Research Plant of Tampere University of Technology (TUT) located in Finland (61.451°N 23.858°E) with 10 Hz frequency. The blue line represents a sunny day, the green line a half-cloudy day, and the black line a cloudy day*

the produced power. Therefore, the probability of a mismatch between the produced power and the demand increases.

As the penetration level of these energy sources becomes more and more prevalent, the reliability, stability, and power quality of the grid degrade if proper actions to overcome these problems are not taken into account. One way to solve these problems is to store energy by using an electrical energy storage (EES), such as a battery. Since EESs can be used to provide grid support and smooth the output of the intermittent renewable energy sources, their research has gained increasing interest over the last years.

Both photovoltaic (PV) and EES systems require power electronic converters in order to be controlled and connected to the grid. Numerous topologies exist for this purpose. The optimized solution is affected by a variety of requirements and limitations, such as the chosen application, rating of the system, and the chosen PV system.

The purpose of this thesis is to provide an insightful and meaningful comparison between the different power electronic topologies utilized in a PV-EES distributed generation (DG) system. In order to make this feasible, the focus is on the following three basic topologies:

(1) Single-stage PV inverter and EES connected to a bi-directional dc-dc converter at the PV generator terminals

(2) Double-stage PV inverter and EES connected to a bi-directional dc-dc converter at the dc-link

(3) Single-stage PV inverter and EES connected to its own inverter

The chosen topologies are compared regarding part count, component sizing, reliability, efficiency, modularity, control system complexity, etc. The comparisons are conducted by analyzing the topologies and performing real-time simulation tests based on the platforms from Typhoon HIL and Imperix.

This thesis is structured as follows. Chapter 2 discusses briefly the characteristics of PV generators (PVGs) and EESs. The required small-signal models are derived. In Chapter 3, the models are combined by integrating the EES with the PV inverters using different topologies. These topologies are then compared according to the aforementioned criteria. The comparisons made are then assessed with simulations in Chapter 4. Finally, Chapter 5 summarizes the highlights of the thesis.

2. GRID-CONNECTED PHOTOVOLTAIC GENERATORS AND AN ENERGY STORAGES

In this chapter, the electrical characteristics of PVGs and EESs are shortly discussed. The small-signal models are derived for current- and voltage-fed inverters, a PV boost converter, and a bi-directional dc-dc converter.

2.1 Photovoltaic Generator

This section presents the working principle of a PV generator. The V-I and V-P characteristics and the maximum power point (MPP) are presented. The perturb and observe (P&O) MPP tracking (MPPT) algorithm is introduced.

A PV generator is internally a power and voltage limited current source. The electrical behavior of the PV cells depends on the environmental factors, such as the irradiance level and the ambient temperature, which makes the modeling demanding compared to other more traditional power sources, such as batteries.

In this thesis, the PV cells are modeled using the one diode model presented in Fig. 2.1. According to the model, the current produced by the PV cell can be expressed as

$$i_{\mathrm{pv}} = i_{\mathrm{ph}} - \underbrace{i_{\mathrm{o}}\left[\exp\left(\frac{v_{\mathrm{pv}} + r_{\mathrm{s}} i_{\mathrm{pv}}}{A v_{\mathrm{t}}}\right) - 1\right]}_{i_d} - \frac{v_{\mathrm{pv}} + r_{\mathrm{s}} i_{\mathrm{pv}}}{r_{\mathrm{sh}}}, \tag{2.1}$$

where i_{ph} is the light generated current, i_{o} the dark saturation current of the cell, v_{pv} the voltage across the cell, r_{s} the parasitic series resistance, r_{sh} the shunt resistance, A the ideality factor, and $v_{\mathrm{t}} = kT/q$ the thermal voltage of the cell, where k is the Boltzmann constant, q the elementary charge, and T the temperature. Finally, i_{d} is the diode resistance.

The electrical characteristics of the PV cell are presented in Fig. 2.2. The solid curve presents the produced current as a function of the voltage across the PV cell

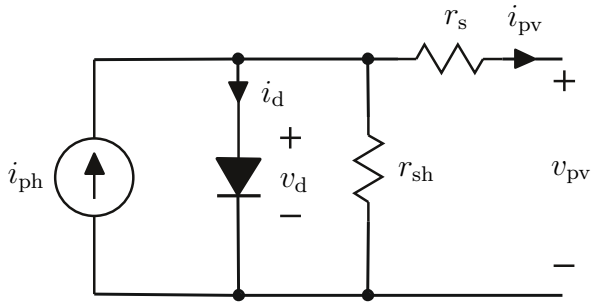

Figure 2.1 *PV cell one diode model.*

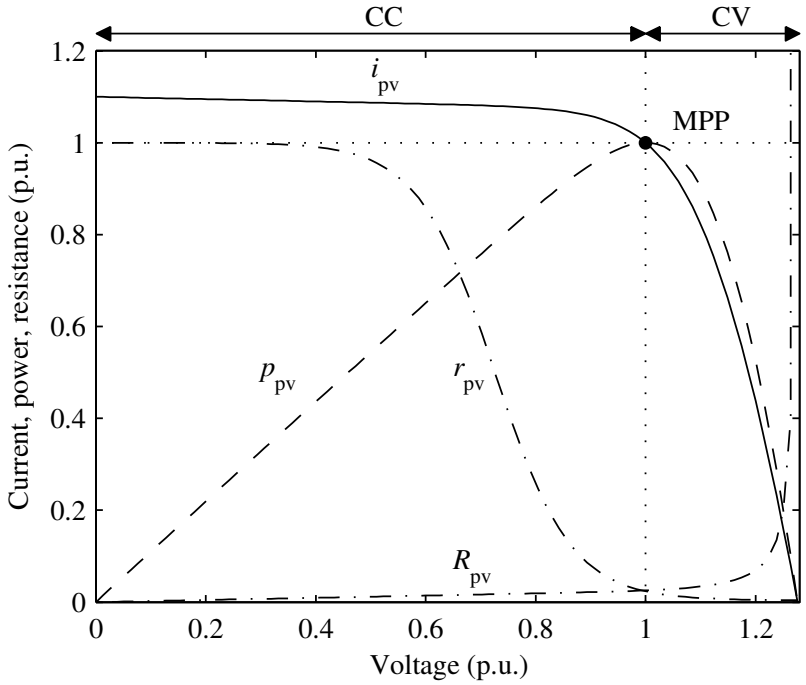

Figure 2.2 *PV current, power, dynamic resistance, and capacitance as a function of voltage relative to the MPP values.*

relative to the maximum power point (MPP) values. This is the operating point at which the highest power is produced. In the constant-current (CC) region (see the figure), the electrical behavior of the PV cell can be considered similar to a constant current source since the variation of the current is relatively small. In the constant-voltage (CV) region (see the figure), the characteristics resemble a constant voltage source since the variation of the voltage is relatively small. At the operating point where the voltage across the PV cell is zero, the PV cell is short-circuited and a short-circuit current flows through it. At the operating point where the current is zero, the PV cell is in open-circuit and the voltage across it is called the open-circuit voltage.

Consequently, the power generated by the PV cell depends on the operating point

as well. The corresponding power, shown in Fig. 2.2 as a dashed line, is normalized based on the maximum power. In addition, the dynamic resistance $r_{\mathrm{pv}} = r_{\mathrm{d}} \| r_{\mathrm{sh}} + r_{\mathrm{s}}$ and static resistance $R_{\mathrm{pv}} = u_{\mathrm{pv}}/i_{\mathrm{pv}}$ are also presented in Fig. 2.2, which are nonlinear and highly dependent on the operating point [25, 29].

Since the current and voltage per cell are considerably low, multiple cells are connected in series and in parallel in order to achieve higher voltage and power levels. Each series connection increases the maximum voltage and each parallel connection increases the maximum current of the system. The MPP voltage across a silicon solar cell is 0.6 V under standard test conditions (25°C and standard AM1.5 illumination of 1 kW/m^2). Typically, one module contains 36 cells set in series, resulting in an open-circuit voltage of 25 V under standard test conditions, and a MPP voltage of 21.6 V.

Since the produced current is most often considerably smaller than the voltage across the PV cell, the variation of the absolute value of the current around the MPP is relatively smaller than that of the voltage. Thus, the MPP current is relatively closer to the short-circuit current than the MPP voltage to the open-circuit voltage. In addition, the MPP current is highly dependent on the irradiance level, which introduces more rapid changes compared to the MPP voltage. The latter, on the other hand, depends mostly on the temperature with only moderate changes. This can be clearly seen in Fig. 2.3 where the MPP current and voltage are presented as a function of irradiance for different temperatures. Therefore, input voltage feedback control is considered as a more appropriate method to control a PV converter compared to input current feedback control, as discussed also in [44]. The control is executed by utilizing an MPPT, which is discussed in Section 2.1.1.

However, when considering the current and voltage across multiple PV cells, the shape of the V-I and V-P curves can vary greatly due to conditions such as partial shading, as discussed in detail, for example, in [23]. When multiple PV cells are connected in series, the PV cell with the lowest short-circuit current limits the current of the whole series connection [42]. In addition, there may be more than one local MPP due to the more complicated shape of the I-V curve, which further complicates the MPPT.

Therefore, in certain situations, such as under partial shading conditions, when the MPP of one or more PV cells is significantly decreased due to partial shading of the cells, the efficiency of the whole system deteriorates. More specifically, this effect is spread to the other non-shaded cells connected in series with the shaded ones, thus the harvested PV power is reduced. These losses are referred to as *mismatching*

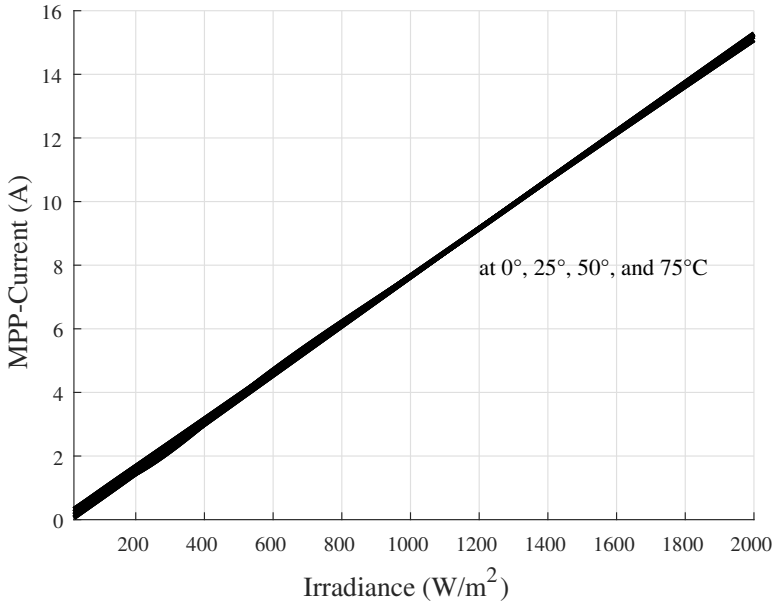

(a) MPP current

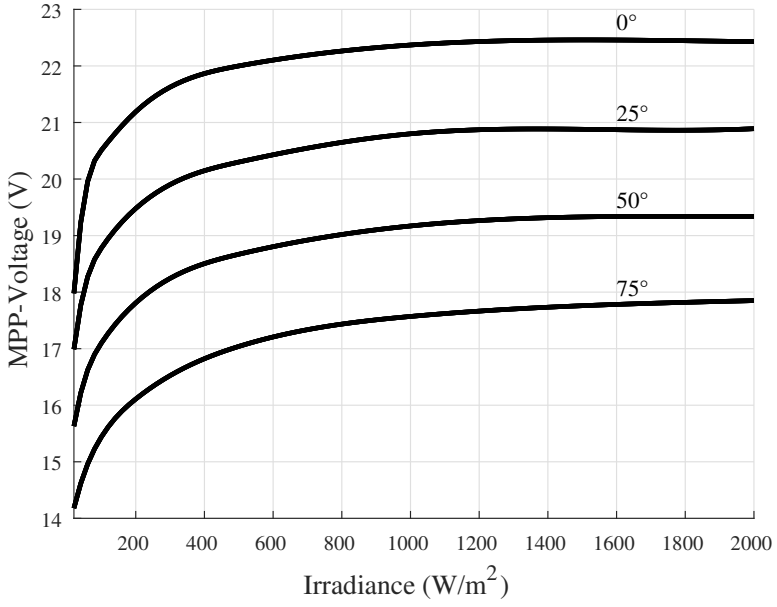

(b) MPP voltage

Figure 2.3 *The MPP current and voltage of a single PV module as a function of irradiance for different temperatures*

losses. Fortunately, they can be reduced moderately by the use of bypass diodes set in parallel with the cells. As discussed in [23], long series connections of PV modules are those most severely affected by partial shading conditions.

The power electronic interfaces of PV systems have two main tasks. First, to control the terminal conditions of the PV module in order to maximize the produced energy.

Secondly, to convert electricity from dc, as produced by the PV array, to ac in order to supply the grid. This should be done at as high efficiency as possible and over a wide range since the irradiance levels are highly fluctuating. The connection to the grid is realized with an inverter. However, an additional dc-dc converter can be placed in between the PV array and the inverter in order to increase the voltage level and thus allow optimized design of the inverter. Both topologies have their advantages and disadvantages, which are discussed in detail in Chapter 3.

2.1.1 Maximum Power Point Tracking

A PV cell produces maximum electricity when it operates at the MPP. This point is subjected to changes in the atmospheric conditions to which the cell is exposed. The goal of the MPPT is to control the switching of the converter in order to adjust its input voltage to match the MPP voltage of the PV array. Various algorithms have been implemented, such as perturb and observe (P&O) algorithm, incremental conductance algorithm, and sliding mode control [22]. In this thesis, only P&O is discussed.

When using P&O MPPT algorithm, the circuit increases or decreases the voltage across the PV array by a small amount Δ_{MPPT} (perturbation) and measures the produced power. If the power increases by an equal amount, the reference voltage V_{ref} is increased or decreased further until the optimal setting is reached. Otherwise, the sign of the perturbation is changed. P&O achieves good efficiency but it can be sluggish and result in oscillations when not properly designed. An example of the algorithm is provided in Figure 2.4.

Due to partial shading conditions, the MPP can vary greatly among the different PV cells and/or modules. Thus, advanced systems process each group individually using, for example, dc-dc converters, in order to avoid mismatching losses. In addition, there may also be more than one local MPP, which calls for even more complex MPPT algorithms in order to track the global MPP. However, P&O is used in this Thesis due to its simplicity.

2.2 Electrical Energy Storage

In this section, the characteristics of different EESs are shortly discussed. However, the focus is on lithium-ion batteries.

There are various technologies to store energy, such as superconducting magnetic energy storages, electric double-layer capacitors, flywheels, batteries (e.g., lead-acid

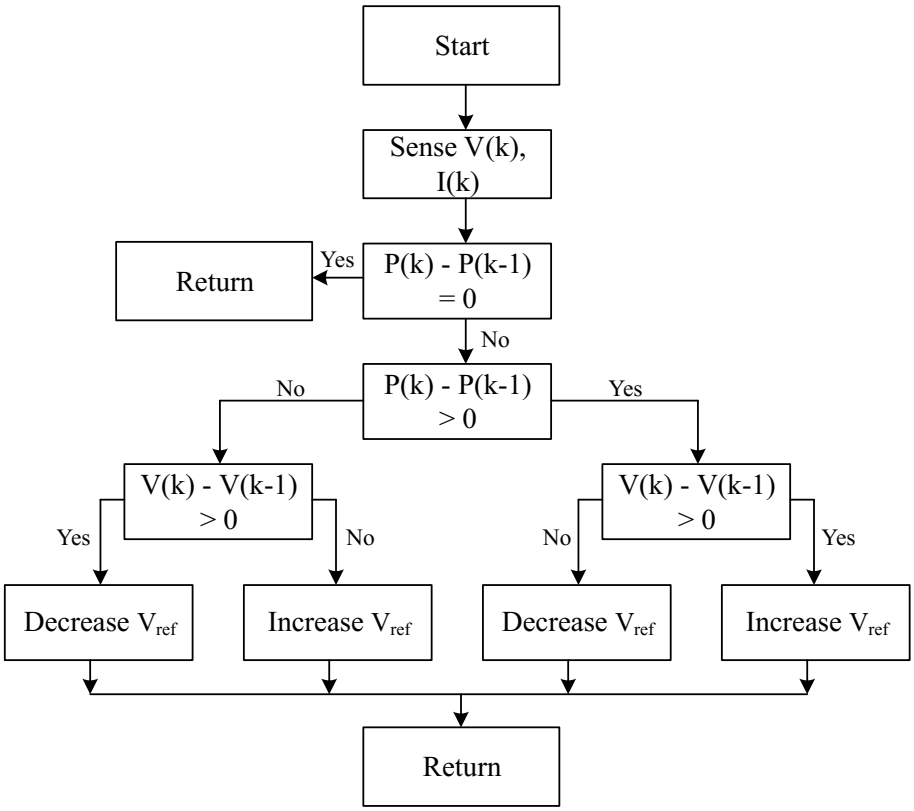

Figure 2.4 *Perturb and observe (P&O) MPPT algorithm.*

batteries, lithium-ion batteries), pumped hydro energy storages, and compressed air energy storages [11]. Each of the source types has its advantages and disadvantages depending on the application. The key performance criteria taken into account when renewable energy integration is of concern include, among others, energy storage capacity, power output, and lifetime [37].

Lithium-ion batteries have become a popular form of EESs due to their high charge and discharge efficiency and high energy density. This can also be seen in Fig. 2.5 where the power and energy densities of various EESs are presented. Moreover, other main advantages of this battery technology are high energy-to-weight ratios, lack of memory effect, and a low self-discharge rate [11, 37].

In lithium-ion batteries, the movement of lithium-ions between the anode and cathode produces a current flow. The battery is charged when the ions move from the metal oxide cathode to the graphitic-carbon anode; motion to the opposite direction discharges the battery [11]. If the battery is charged at a rate faster than lithium can homogenize in an active particle by diffusion, this inhomogeneous distribution of lithium causes stress which may fracture the particle [45]. In addition, the internal resistance can produce internal heat-up and failure and the batteries are very sensi-

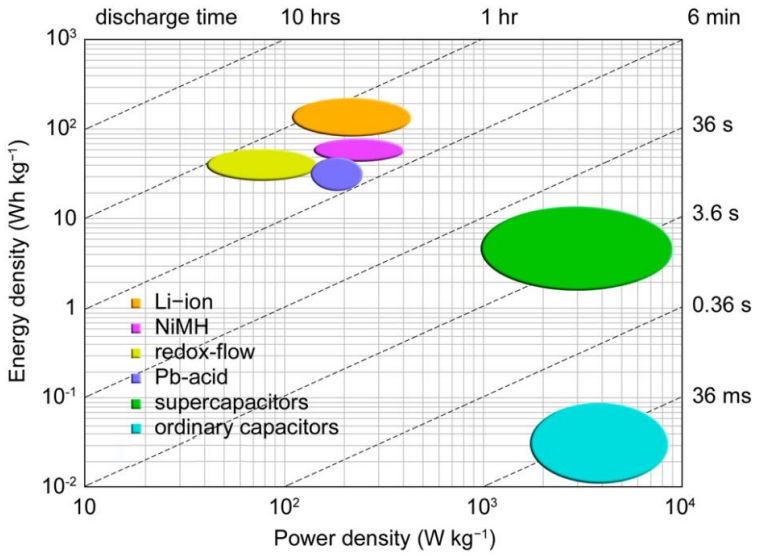

Figure 2.5 *Power and energy densities of different EESs [9]*

tive to over- and undercharge. Therefore, to ensure safe operation, it is necessary to use a battery management system to provide at least over-voltage, under-voltage, over-temperature, and over-current protection [37].

Battery voltage varies depending on multiple factors, such as, the state-of-charge (SoC). The battery terminal voltage can be modeled as

$$v_{\text{batt}} = N_{\text{s}} \cdot E_0 - N_{\text{s}} \cdot K \frac{N_{\text{p}} \cdot Q}{N_{\text{p}} \cdot Q - Q_{\text{t}}} + N_{\text{s}} \cdot A \cdot e^{-N_{\text{p}} \cdot B \cdot Q_{\text{t}}} - R_{\text{int}} \cdot i_{\text{batt}} \ , \tag{2.2}$$

where v_{batt} is the battery terminal voltage, N_{s} and N_{p} are the numbers of series and parallel connected cells with the capacity Q per cell, E_0 is the battery constant voltage, K is the polarisation voltage, $Q_{\text{t}} = \int i_{\text{batt}} \text{dt}$ is the actual battery charge, A is the exponential zone amplitude (V), B is the exponential zone time constant inverse (Ah^{-1}), R_{int} is the internal resistance, and i_{batt} is the battery current. Further information about this model, such as how to extract the model parameters, can be found, for example, in [24, 34]. The relation between the battery charge and the battery terminal voltage is demonstrated in Fig 2.6.

Based on the desired power P_{batt}, the current can be given as

$$i_{\text{batt}} = \frac{P_{\text{batt}}}{v_{\text{batt}}}. \tag{2.3}$$

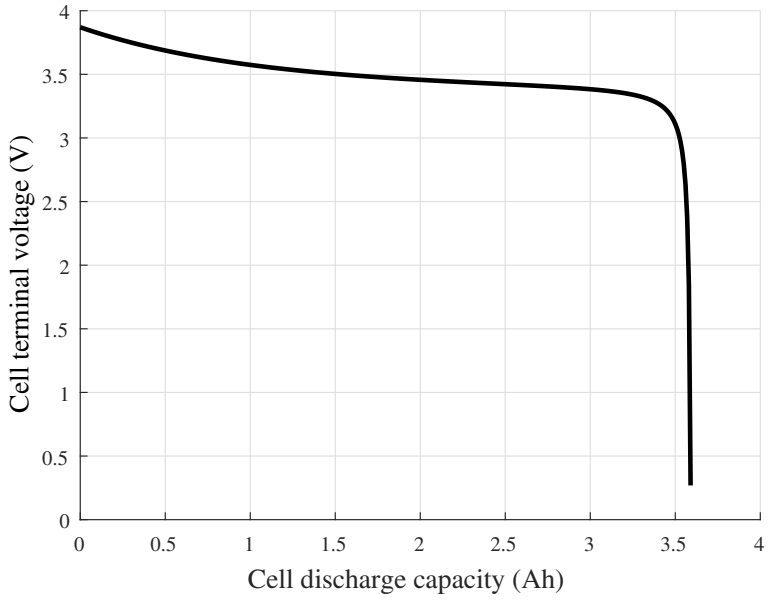

Figure 2.6 *The battery terminal voltage as a function of the discharge capacity for a lithium-ion battery cell*

The SoC (%) can be determined as

$$\mathrm{SoC} = 1 - \frac{Q_\mathrm{t}}{N_\mathrm{p} \cdot Q}. \tag{2.4}$$

Battery discharge current is indicated with a C-rate, which is a measure of the rate at which the battery is discharged with respect to its maximum capacity [33]. A C-rate of 1C means that the discharge current will discharge the entire battery in 1 hour. For a battery with a capacity of 100 Ah, this equates to a discharge current of 100 A. Forcing ultra-fast charging adds stress, even if the battery is designed for such a purpose. Thus, in order to secure a long lifetime for the battery, the current should be limited. Commonly, with lithium-ion batteries, a limit of 1C is considered a good limitation for this purpose, with an absolute maximum of 2C [8]. The battery current limits can be calculated based on the C-rate according to

$$i_{\mathrm{batt-max}} = C_\mathrm{r} N_\mathrm{p} Q_\mathrm{cell}, \tag{2.5}$$

where C_r is the C-rate.

The number of battery cells demanded depends on the full operating power requirements. The current depends on the battery voltage at the same conditions. In Fig 2.7 are shown the power and current as a function of C-rate when 200 V voltage is assumed. Thus, the power presented in this figure can be preserved as long as the voltage does not decrease lower than 200 V. It should be noted, that

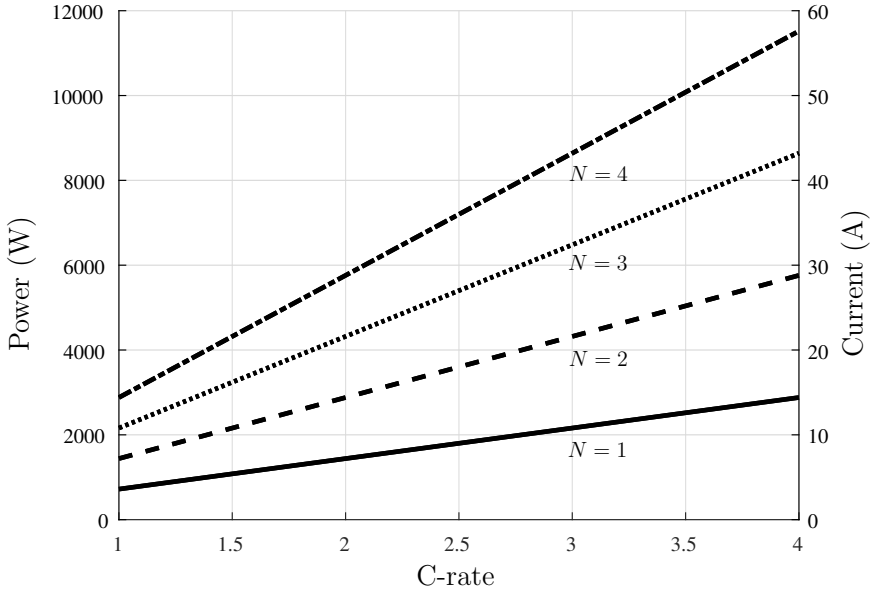

Figure 2.7 *The maximum allowed current and the power it produces as a function of the C-rate with N 3.6 Ah batteries connected in parallel. The battery voltage is assumed to be 200 V for all the cases*

if the power needs to be increased, it can be achieved not only by increasing the C-rate or setting more batteries in parallel, but also by setting more batteries in series and, thus, increasing the voltage.

In order to avoid the battery cells discharging on their own it is important that the voltages and charges of the cells are close to each other. Therefore, battery packs utilize a battery management system (BMS) controller which estimates the SoC and state of health (SoH) of each battery cell and applies charge equalization to balance the charge of all the cells in the pack [30]. The most important task of a BMS is to protect the battery cells from overcharge and undercharge.

Most often, EESs require an additional equipment to adapt their output voltage or current to the required level. This is the case with batteries, since their dc output has to be converted to the ac voltage level of the grid. Depending on the application, the power converter has to allow the connection between two different dc buses or a dc voltage bus and an ac voltage bus. Methods to achieve these are presented in Sections 2.3 and 2.5.

There are various approaches to utilize grid-connected EESs. As discussed in Chapter 1, the intermittent nature of the two fast growing energies, i.e., wind and solar, cause voltage and frequency fluctuations in the grid and increase the potential for unbalance between power generation and demand. PV generation systems cannot meet the grid and user requirements for power quality if they depend only on their

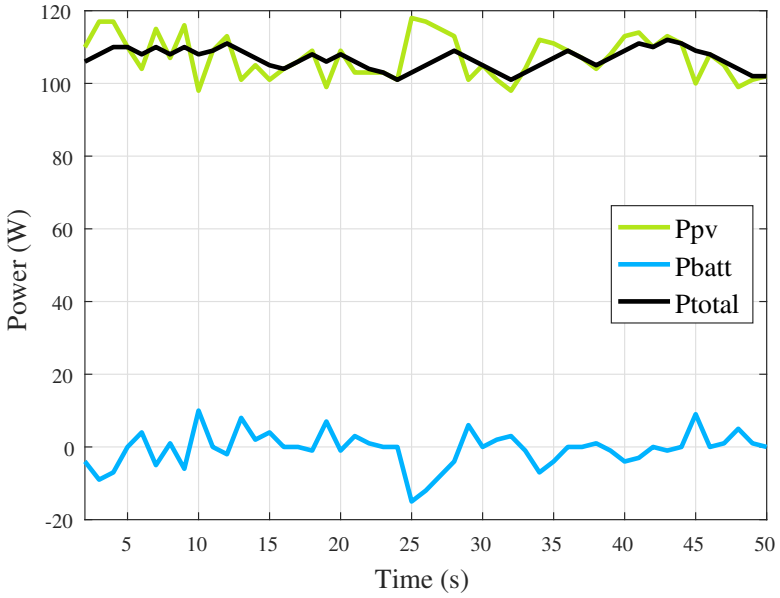

Figure 2.8 *The idea of ramp-rate control using a battery to compensate for the power produced by PV panels. The derivative of the total power is limited to 2 W/s*

own power supply capacity [12].

EESs can be used, for example, for *load leveling*, which refers to the usage of EES to supply peak electricity demand by charging the EES during low demand and discharging during high demand, as demonstrated in [38]. EES can be a potential alternative to peaking power instead of using, for example, gas turbines. *Energy arbitrage* refers to earning profit by charging EES with cheap electricity and selling the stored energy at a higher price during peak demand [37], thus optimizing the profit.

The rapid power changes in PV power plants produce voltage fluctuations, which can be reduced with EESs by *intermittency mitigation*, i.e., by matching the supply to the demand [37, 31]. This has been demonstrated, for example, in [18]. The fluctuations in the PV power can be smoothened by utilizing *a ramp-rate control scheme*, in which the EES charges and discharges in a way that compensates only for the fluctuations that have higher derivative than a chosen limit. The idea of this control is presented in Fig. 2.8. Also blackouts and other long-period interruptions can be prevented by utilizing EESs. As a result, the reliability of the grid can be further increased.

Unlike conventional synchronous generators, such as gas or steam turbines, PV power plants do not normally provide any rotational inertia. This creates yet another

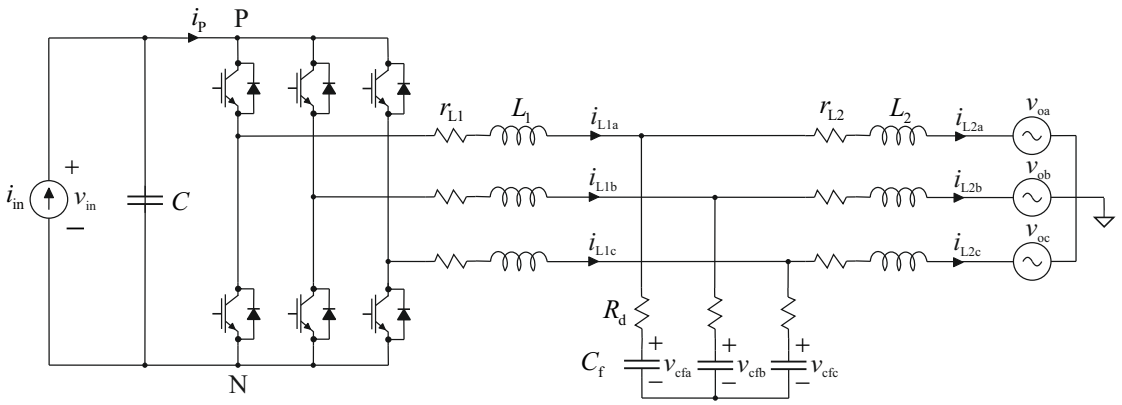

Figure 2.9 *Current-fed inverter with LCL-type output filter*

application of EESs to provide inertia emulation [37]. Due to their fast response behavior, batteries are suitable for providing either fast frequency (and voltage) control or synthetic rotational inertia [35].

2.3 Small-Signal Modeling of a Photovoltaic Inverter

In this thesis, the inverters are analyzed as two-level three-phase inverters. *LCL*-type filters are used to filter out the switching ripples. The PV inverter is depicted in Fig. 2.9. The filter inductors are depicted with L_1 and L_2 and their equivalent series resistances with r_{L1} and r_{L2}, respectively. The filter capacitor is depicted with C_f and the symbol R_d is used to depict the combination of the filter-capacitor equivalent series resistance (ESR) value and the damping resistor. The dc-side capacitor is depicted with C. As justified in Section 2.1, the converters in PV applications control usually their input voltages. Thus, they are analyzed as current-fed current-output converters.

Inverters are generally controlled with decoupled d-q vector control. Various other controlling methods have also been developed, such as proportional resonant control, model predictive control, and even control methods based on artificial neural networks, demonstrated in [21, 20, 17], respectively. However, in this thesis, only the standard d-q control is applied.

Since the upper and lower switches are switched in a complementary manner, it is sufficient to model only the duty ratios of the upper switches as system inputs. The

state, input, and output vectors are chosen as

$$\begin{aligned}
\boldsymbol{x} &= \begin{bmatrix} i_{\mathrm{L1d}} & i_{\mathrm{L1q}} & i_{\mathrm{L2d}} & i_{\mathrm{L2q}} & v_{\mathrm{Cfd}} & v_{\mathrm{Cfq}} & v_{\mathrm{C}} \end{bmatrix}^T \\
\boldsymbol{u} &= \begin{bmatrix} i_{\mathrm{in}} & v_{\mathrm{od}} & v_{\mathrm{oq}} & d_{\mathrm{d}} & d_{\mathrm{q}} \end{bmatrix}^T \\
\boldsymbol{y} &= \begin{bmatrix} v_{\mathrm{in}} & i_{\mathrm{L1d}} & i_{\mathrm{L1q}} & i_{\mathrm{L2d}} & i_{\mathrm{L2q}} \end{bmatrix}^T,
\end{aligned} \tag{2.6}$$

where i_{L1d} and i_{L1q} are the inverter current d and q components, respectively, i_{L2d} and i_{L2q} the grid current d and q components, respectively, v_{Cfd} and v_{Cfq} the d and q components of the voltage across the filter capacitor, respectively, v_{od} and v_{oq} are the grid voltage d and q components, respectively, d_{d} and d_{q} the modulation index d and q components, respectively, and v_{C} is the voltage across the input capacitor, v_{in} the voltage across the input source, and i_{in} the input source current.

In order to model the inverter, the moving average in state space model is used [10]. The method is widely used for modeling of switched power converters operating with sinusoidal pulse width modulation (SPWM) control. It consists of obtaining the weighted average state of the circuit with respect to the operating duty cycle over a switching period. In order to derive the average model of the system, the Kirchoff's voltage and current laws are utilized to derive the differential equations that describe the dynamics of the system. Then, the steady state operating point can be determined by setting the derivatives to zero and substituting all variables with their corresponding steady-state values.

Finally, according to [10], a linear model of the converter is derived to describe its behavior to small variations around the operating point. This is done by linearizing the average model at the steady-state operating point by using the first-order expansion of the Taylor series. Thus, the small-signal dynamics are given in state space form

$$\begin{aligned}
\dot{\boldsymbol{x}} &= \boldsymbol{A}\boldsymbol{x} + \boldsymbol{B}\boldsymbol{u} \\
\boldsymbol{y} &= \boldsymbol{C}\boldsymbol{x} + \boldsymbol{D}\boldsymbol{u},
\end{aligned} \tag{2.7}$$

where the matrices $\boldsymbol{A}$, $\boldsymbol{B}$, $\boldsymbol{C}$, and $\boldsymbol{D}$ are defined as

$$
\begin{aligned}
\boldsymbol{A} &= \begin{bmatrix}
-\frac{r_{\mathrm{L1}}+R_{\mathrm{d}}}{L_1} & \omega_{\mathrm{s}} & \frac{R_{\mathrm{d}}}{L_1} & 0 & -\frac{1}{L_1} & 0 & \frac{D_{\mathrm{d}}}{L_1} \\
-\omega_{\mathrm{s}} & -\frac{r_{\mathrm{L1}}+R_{\mathrm{d}}}{L_1} & 0 & \frac{R_{\mathrm{d}}}{L_1} & 0 & -\frac{1}{L_1} & \frac{D_{\mathrm{q}}}{L_1} \\
\frac{R_{\mathrm{d}}}{L_2} & 0 & -\frac{r_{\mathrm{L2}}+R_{\mathrm{d}}}{L_2} & \omega_{\mathrm{s}} & \frac{1}{L_2} & 0 & 0 \\
0 & \frac{R_{\mathrm{d}}}{L_2} & -\omega_{\mathrm{s}} & -\frac{r_{\mathrm{L2}}+R_{\mathrm{d}}}{L_2} & 0 & \frac{1}{L_2} & 0 \\
\frac{1}{C_{\mathrm{f}}} & 0 & -\frac{1}{C_{\mathrm{f}}} & 0 & 0 & \omega_{\mathrm{s}} & 0 \\
0 & \frac{1}{C_{\mathrm{f}}} & 0 & -\frac{1}{C_{\mathrm{f}}} & -\omega_{\mathrm{s}} & 0 & 0 \\
-\frac{3D_{\mathrm{d}}}{2C} & -\frac{3D_{\mathrm{q}}}{2C} & 0 & 0 & 0 & 0 & 0
\end{bmatrix} \\
\boldsymbol{B} &= \begin{bmatrix}
0 & 0 & 0 & \frac{V_{\mathrm{in}}}{L_1} & 0 \\
0 & 0 & 0 & 0 & \frac{V_{\mathrm{in}}}{L_1} \\
0 & -\frac{1}{L_2} & 0 & 0 & 0 \\
0 & 0 & -\frac{1}{L_2} & 0 & 0 \\
0 & 0 & 0 & 0 & 0 \\
0 & 0 & 0 & 0 & 0 \\
\frac{1}{C} & 0 & 0 & -\frac{3I_{\mathrm{L1d}}}{2C} & -\frac{3I_{\mathrm{L1q}}}{2C}
\end{bmatrix} \\
\boldsymbol{C} &= \begin{bmatrix}
0 & 0 & 0 & 0 & 0 & 0 & 1 \\
1 & 0 & 0 & 0 & 0 & 0 & 0 \\
0 & 1 & 0 & 0 & 0 & 0 & 0 \\
0 & 0 & 1 & 0 & 0 & 0 & 0 \\
0 & 0 & 0 & 1 & 0 & 0 & 0
\end{bmatrix} \\
\boldsymbol{D} &= \begin{bmatrix} 0 \end{bmatrix}_{5\times 5}.
\end{aligned}
\tag{2.8}
$$

The capital letters refer to the steady-state values and the dot above a variable refers to its time-derivative. By utilizing the Laplace transformation, the open-loop transfer functions from $\hat{d}_{\mathrm{d}}$ to $\hat{i}_{\mathrm{L1d}}$ ($G_{\mathrm{cLdd-o}}$), $\hat{d}_{\mathrm{q}}$ to $\hat{i}_{\mathrm{L1q}}$ ($G_{\mathrm{cLqq-o}}$), and $\hat{d}_{\mathrm{d}}$ to $\hat{v}_{\mathrm{in}}$

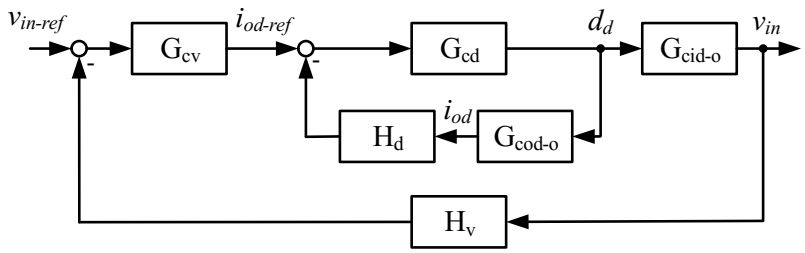

(a) Input voltage and output current d-component control (cascaded control scheme)

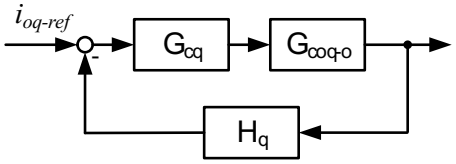

(b) Output current q-component control

Figure 2.10 *Control block diagrams of a VSI inverter controlling its input voltage and output currents*

($G_{\mathrm{cid-o}}$) can be solved from $\boldsymbol{G} = \boldsymbol{C}(s\boldsymbol{I} - \boldsymbol{A})^{-1}\boldsymbol{B} + \boldsymbol{D}$, i.e.

$$\boldsymbol{Y} = \boldsymbol{G}\boldsymbol{U} = \begin{bmatrix} Z_{\mathrm{in-o}} & T_{\mathrm{oid-o}} & T_{\mathrm{oiq-o}} & G_{\mathrm{cid-o}} & G_{\mathrm{ciq-o}} \\ G_{\mathrm{iLd-o}} & T_{\mathrm{oLdd-o}} & T_{\mathrm{oLqd-o}} & G_{\mathrm{cLdd-o}} & G_{\mathrm{cLqd-o}} \\ G_{\mathrm{iLq-o}} & T_{\mathrm{oLdq-o}} & T_{\mathrm{oLqq-o}} & G_{\mathrm{cLdq-o}} & G_{\mathrm{cLqq-o}} \\ G_{\mathrm{iod-o}} & -Y_{\mathrm{odd-o}} & -Y_{\mathrm{oqd-o}} & G_{\mathrm{codd-o}} & G_{\mathrm{coqd-o}} \\ G_{\mathrm{ioq-o}} & -Y_{\mathrm{odq-o}} & -Y_{\mathrm{oqq-o}} & G_{\mathrm{codq-o}} & G_{\mathrm{coqq-o}} \end{bmatrix} \boldsymbol{U}, \tag{2.9}$$

where the Z, Y, G, and T, depict the transfer functions between the input and output variables.Note, that the inverter output current i_{L1} is usually controlled instead of the grid current i_{L2} in order to limit the inverter current within safety limits.

As discussed in [25], appearance of a right half-plane (RHP) zero and change of sign in $G_{\mathrm{codd-o}}$ when changing between CC and CV regions causes stability issues. Specifically, the output current control cannot be stable in both the CC and CV regions. Thus, the grid current and the dc-side voltage need to be controlled in a cascaded manner, where v_{in} is controlled in the outer loop and i_{L1d} in the inner loop. The control block diagram is presented in Fig. 2.10. The control method enables the operation at all operating points and makes it possible to utilize the MPPT in a reliable manner.

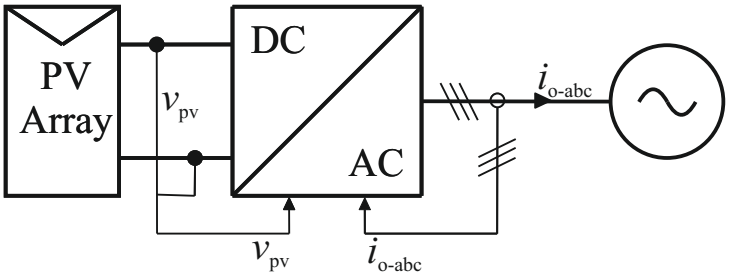

(a) Grid-feeding/supporting mode

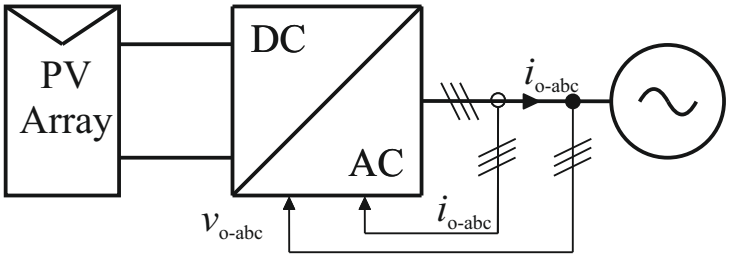

(b) Grid-forming mode

Figure 2.11 *Possible operation modes of single-stage grid-connected PV energy system*

Another possibility is to use the inverter to control both the grid current and the grid voltage. This is called grid-forming mode, since the inverter contributes to the voltage and frequency stability of the grid. The differences between the control methods for the single-stage topology are shown in Fig. 2.11. It is evident that in order to control the PV voltage, and thus to utilize the MPPT in grid-forming mode, a double-stage topology is necessary.

Since the EESs behave as a dc voltage source, it requires an inverter in order to feed an ac grid. The converters need to be bi-directional in order to achieve both charging and discharging of the EES. The topology for this is shown in Fig. 2.12. It is the same as in Fig. 2.9 except that the source is a constant voltage source instead of a constant current source and the input capacitor is not required. The inverter works as a rectifier when the power is transferred from the ac grid to dc source and as an inverter when the power is transferred from the dc source to the ac grid. The dynamics can be solved the same way as done for the current source case. However,

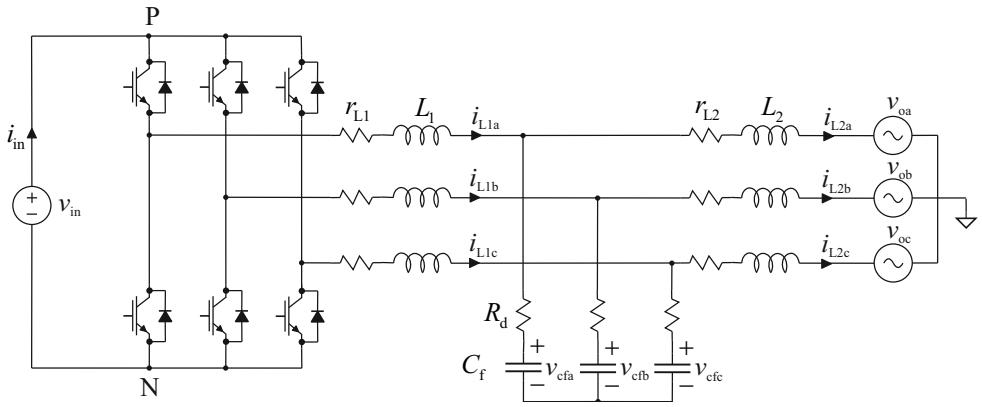

Figure 2.12 *Voltage source inverter*

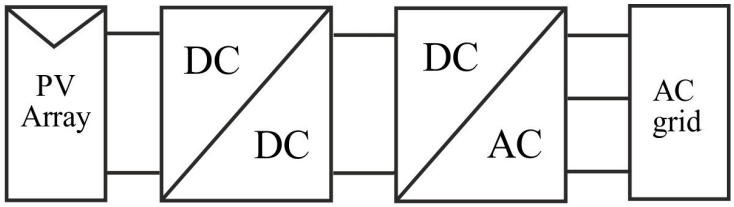

Figure 2.13 *Double-stage PV inverter*

in this case, the state, input, and output vectors should be chosen as

$$\begin{aligned} \boldsymbol{x} &= \begin{bmatrix} i_{\mathrm{L1d}} & i_{\mathrm{L1q}} & i_{\mathrm{L2d}} & i_{\mathrm{L2q}} & v_{\mathrm{Cfd}} & v_{\mathrm{Cfq}} \end{bmatrix}^T \\ \boldsymbol{u} &= \begin{bmatrix} v_{\mathrm{in}} & v_{\mathrm{od}} & v_{\mathrm{oq}} & d_{\mathrm{d}} & d_{\mathrm{q}} \end{bmatrix}^T \\ \boldsymbol{y} &= \begin{bmatrix} i_{\mathrm{in}} & i_{\mathrm{L1d}} & i_{\mathrm{L1q}} & i_{\mathrm{L2d}} & i_{\mathrm{L2q}} \end{bmatrix}^T . \end{aligned} \tag{2.10}$$

2.4 Small-Signal Modeling of a Photovoltaic Boost Converter

In double-stage PV systems, a dc-dc converter is inserted in between the grid-interfacing inverter and the PV generator, as shown in Fig. 2.13. The dc-dc converter is responsible for the MPPT function. This is achieved by controlling its input voltage, i.e., the voltage across the PV array. The VSI-type inverter has a similar cascaded control structure as in the single-stage scheme presented in Section 2.3. However, its main function is to control the dc-link voltage instead of performing MPPT. Thus, both the dc-dc and the dc-ac converters control their input voltages and, therefore, they must be analyzed as current-fed current-output converters.

The dc-dc converter is typically a boost converter with an additional input capacitor.

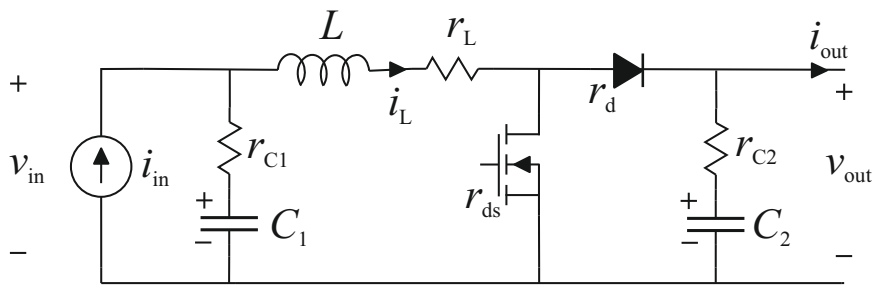

Figure 2.14 *PV boost converter*

The topology is shown in Fig. 2.14. In order to model the boost converter, the moving average in state space method—introduced in Section 2.3—is applied. The state, input, and output vectors are chosen as

$$\begin{aligned} \boldsymbol{x} &= \begin{bmatrix} i_{\mathrm{L}} & v_{\mathrm{C1}} & v_{\mathrm{C2}} \end{bmatrix}^T \\ \boldsymbol{u} &= \begin{bmatrix} i_{\mathrm{in}} & v_{\mathrm{out}} & d \end{bmatrix}^T \\ \boldsymbol{y} &= \begin{bmatrix} v_{\mathrm{in}} & i_{\mathrm{out}} \end{bmatrix}^T . \end{aligned} \tag{2.11}$$

By utilizing Kirchoff's voltage and current laws in order to solve the derivatives of the state and output variables and averaging these equations over one switching cycle, the average model of the system is

$$\begin{aligned} \frac{d\langle i_{\mathrm{L}}\rangle}{dt} &= \frac{-(r_{\mathrm{C1}} + r_{\mathrm{L}} + dr_{\mathrm{ds}} + d'r_{\mathrm{d}})}{L}\langle i_{\mathrm{L}}\rangle - \frac{d'}{L}\langle v_{\mathrm{out}}\rangle + \frac{1}{L}\langle v_{\mathrm{C1}}\rangle \\ &\quad + \frac{r_{\mathrm{C1}}}{L}\langle i_{\mathrm{in}}\rangle - \frac{d'}{L}V_{\mathrm{D}} \\ \frac{d\langle v_{\mathrm{C1}}\rangle}{dt} &= -\frac{1}{C_1}\langle i_{\mathrm{L}}\rangle + \frac{1}{C_1}\langle i_{\mathrm{in}}\rangle \\ \frac{d\langle v_{\mathrm{C2}}\rangle}{dt} &= \frac{1}{r_{\mathrm{C2}}C_2}\langle v_{\mathrm{C2}}\rangle + \frac{1}{r_{\mathrm{C2}}C_2}\langle v_{\mathrm{out}}\rangle \\ \langle v_{\mathrm{in}}\rangle &= -r_{\mathrm{C1}}\langle i_{\mathrm{L}}\rangle + \langle v_{\mathrm{C1}}\rangle + r_{\mathrm{C1}}\langle i_{\mathrm{in}}\rangle \\ \langle i_{\mathrm{out}}\rangle &= d'\langle i_{\mathrm{L}}\rangle + \frac{1}{r_{\mathrm{C2}}}\langle v_{\mathrm{C2}}\rangle - \frac{1}{r_{\mathrm{C2}}}\langle v_{\mathrm{out}}\rangle. \end{aligned} \tag{2.12}$$

By setting the derivatives to zero and substituting all variables with their corresponding steady-state values (depicted with the upper-case letters), the steady state

operating point can be determined as

$$\begin{aligned} D' &= \frac{V_{\text{in}} - (r_{\text{sw}} + r_{\text{L}})I_{\text{in}}}{V_{\text{out}} + V_{\text{D}} - (r_{\text{sw}} - r_{\text{D}})I_{\text{in}}}, \\ D &= 1 - D', \\ V_{\text{in}} &= V_{\text{C1}}, \\ V_{\text{C2}} &= V_{\text{out}}, \\ I_{\text{out}} &= D' I_{\text{in}}. \end{aligned} \tag{2.13}$$

Finally, the linear model of the boost converter that describes its behavior to small variations around the operating point is obtained by linearizing (2.12) at the steady-state operating point by using the first-order expansion of the Taylor series. Thus, the small-signal dynamics can be derived as

$$\begin{aligned} \frac{d\hat{i}_{\text{L}}}{dt} &= \frac{-(r_{\text{C1}} + r_{\text{L}} + D r_{\text{ds}} + D' r_{\text{d}})}{L}\hat{i}_{\text{L}} - \frac{D'}{L}\hat{v}_{\text{out}} + \frac{1}{L}\hat{v}_{\text{C1}} \\ &\quad + \frac{r_{\text{C1}}}{L}\hat{i}_{\text{in}} + \left(\frac{V_{\text{out}} + V_{\text{D}}}{L} - I_{\text{L}}\frac{r_{\text{ds}} - r_{\text{d}}}{L}\right)\hat{d} \\ \frac{d\hat{v}_{\text{C1}}}{dt} &= -\frac{1}{C_1}\hat{i}_{\text{L}} + \frac{1}{C_1}\hat{i}_{\text{in}} \\ \frac{d\hat{v}_{\text{C2}}}{dt} &= \frac{1}{r_{\text{C2}}C_2}\hat{v}_{\text{C2}} + \frac{1}{r_{\text{C2}}C_2}\hat{v}_{\text{out}} \\ \hat{v}_{\text{in}} &= -r_{\text{C1}}\hat{i}_{\text{L}} + \hat{v}_{\text{C1}} + r_{\text{C1}}\hat{i}_{\text{in}} \\ \hat{i}_{\text{out}} &= D'\hat{i}_{\text{L}} + I_{\text{L}}\hat{d} + \frac{1}{r_{\text{C2}}}\hat{v}_{\text{C2}} - \frac{1}{r_{\text{C2}}}\hat{v}_{\text{out}}, \end{aligned} \tag{2.14}$$

where the hat symbols refer to small variations around the operating point and the capital letters to the steady-state values. The dynamics can be obtained by solving the transfer functions between the input and output variables in the frequency domain. Utilizing Laplace transformation, the converter open-loop dynamics can be presented with transfer functions as

$$\begin{bmatrix} \hat{u}_{\text{in}} \\ \hat{i}_{\text{out}} \end{bmatrix} = \begin{bmatrix} Z_{\text{in-o}} & T_{\text{oi-o}} & G_{\text{ci-o}} \\ G_{\text{io-o}} & -Y_{\text{o-o}} & G_{\text{co-o}} \end{bmatrix} \begin{bmatrix} \hat{i}_{\text{in}} \\ \hat{u}_{\text{out}} \\ \hat{d} \end{bmatrix}. \tag{2.15}$$

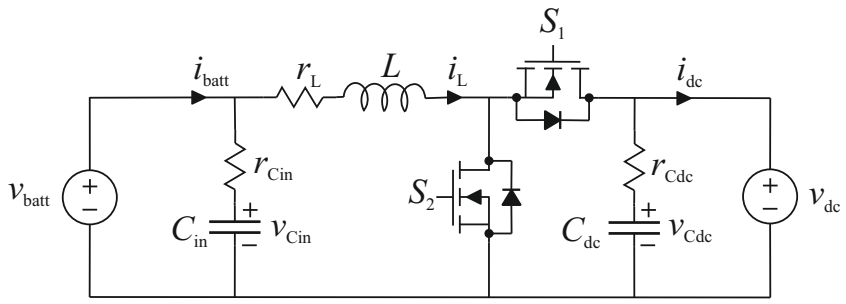

Figure 2.15 *Bi-directional dc-dc converter*

2.5 Small-Signal Modeling of a Bi-Directional DC-DC Converter

By adding an additional dc-dc conversion stage between the battery and the dc-link of the inverter, higher voltage conversion stage can be achieved. Uni-directional dc-dc converters do not allow reverse current flow since they have diodes in their topology. However, for example, by replacing the diodes with controllable switches, the topologies can be turned into bi-directional converters. Since the battery needs to be both charged and discharged, both voltage step up and step down modes are required depending on the direction of the current. When the battery is discharging, the current flows from the battery to the converter output and the converter increases the voltage. When the battery is charging, the current flows from the converter output to the battery and the converter decreases the voltage.

The bi-directional converter presented in Fig. 2.15 is often utilized in battery applications due to its simplicity. It operates as a boost converter while discharging (S_1 non-active and S_2 switching) and as a buck converter while charging (S_2 non-active and S_1 switching). The operation modes are shown in Fig. 2.16. In boost operation mode, the power flow direction is from the battery to the output, and in buck operation mode, the power flow direction is from the output to the battery. The inductor is on the low-voltage side, into which the battery is connected. Its function is to decrease the current ripple.

By comparing the mode on- and off-time topologies, it can be noticed, that the two modes are complementary: The on-time of the buck operation mode corresponds to the off-time of the boost operation mode, and vice versa. Thus, it is possible to derive a model that represents both the operation modes. This has been explained,

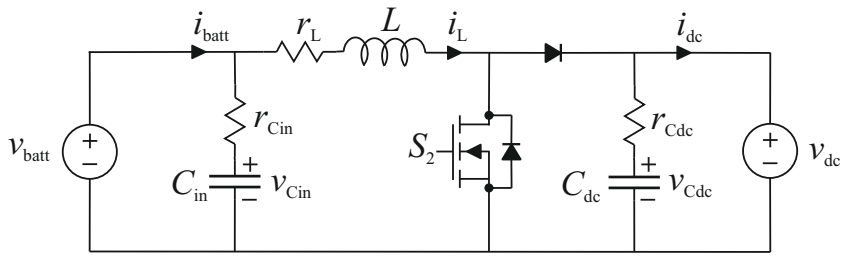

(a) Boost mode

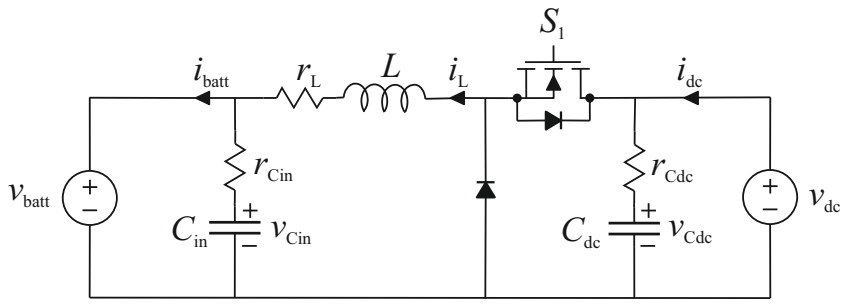

(b) Buck mode

Figure 2.16 *Operation modes of the bi-directional dc-dc converter*

for example, in [27]. Therefore, only the small-signal model for the buck operation mode is derived here, and the model for the boost operation is attained by reversing the low voltage (battery) and the higher voltage side parameters as well as the direction of the current. Moreover, the duty ratio equal to d in the boost mode is replaced by its complementary, i.e., $1 - d$, which corresponds to the duty ratio in buck mode.

The state, output, and input vectors are chosen as

$$\boldsymbol{x} = \begin{bmatrix} v_{\mathrm{Cdc}} \\ v_{\mathrm{Cin}} \\ i_{\mathrm{L}} \end{bmatrix}, \ \boldsymbol{u} = \begin{bmatrix} v_{\mathrm{dc}} \\ v_{\mathrm{batt}} \\ d \end{bmatrix}, \text{ and } \boldsymbol{y} = \begin{bmatrix} i_{\mathrm{batt}} \\ i_{\mathrm{L}} \\ i_{\mathrm{dc}} \end{bmatrix}. \tag{2.16}$$

The dynamic equations for the buck operation mode during on-time are

$$\begin{aligned}
\frac{dv_{\mathrm{Cdc}}}{dt} &= \frac{1}{C_{\mathrm{dc}}} i_{\mathrm{L}} - \frac{1}{C_{\mathrm{dc}}} i_{\mathrm{dc}} \\
\frac{dv_{\mathrm{Cin}}}{dt} &= -\frac{1}{C_{\mathrm{in}} r_{\mathrm{Cin}}} v_{\mathrm{Cin}} + \frac{1}{C_{\mathrm{in}} r_{\mathrm{Cin}}} v_{\mathrm{batt}} \\
\frac{di_{\mathrm{L}}}{dt} &= -\frac{1}{L} v_{\mathrm{Cdc}} - \frac{r_{\mathrm{L}} + r_{\mathrm{Cdc}}}{L} i_{\mathrm{L}} + \frac{r_{\mathrm{Cdc}}}{L} i_{\mathrm{dc}} + \frac{1}{L} v_{\mathrm{batt}} \\
i_{\mathrm{batt}} &= i_{\mathrm{L}} - C_{\mathrm{in}} \frac{\mathrm{d}v_{\mathrm{Cin}}}{\mathrm{d}t} \\
i_{\mathrm{L}} &= i_{\mathrm{L}} \\
i_{\mathrm{dc}} &= i_{\mathrm{L}} - C_{\mathrm{dc}} \frac{\mathrm{d}v_{\mathrm{Cdc}}}{\mathrm{d}t}.
\end{aligned} \tag{2.17}$$

Correspondingly, the dynamic equations for the buck operation mode during off-time are

$$\begin{aligned}
\frac{dv_{\mathrm{Cdc}}}{dt} &= -\frac{1}{C_{\mathrm{dc}}} i_{\mathrm{dc}} \\
\frac{dv_{\mathrm{Cin}}}{dt} &= -\frac{1}{C_{\mathrm{in}} r_{\mathrm{Cin}}} v_{\mathrm{Cin}} + \frac{1}{C_{\mathrm{in}} r_{\mathrm{Cin}}} v_{\mathrm{batt}} \\
\frac{di_{\mathrm{L}}}{dt} &= -\frac{r_{\mathrm{L}}}{L} i_{\mathrm{L}} + \frac{1}{L} v_{\mathrm{batt}} \\
i_{\mathrm{batt}} &= i_{\mathrm{L}} + C_{\mathrm{in}} \frac{\mathrm{d}v_{\mathrm{Cin}}}{\mathrm{d}t} \\
i_{\mathrm{L}} &= i_{\mathrm{L}} \\
i_{\mathrm{dc}} &= -C_{\mathrm{dc}} \frac{\mathrm{d}v_{\mathrm{Cdc}}}{\mathrm{d}t}.
\end{aligned} \tag{2.18}$$

As done, for example, in Section 2.4, by averaging the equations over one switching cycle, linearizing the averaged model at the steady-state, and employing Laplace transformation, the transfer functions can be solved as

$$\boldsymbol{y} = \begin{bmatrix} Y_{\mathrm{in-o}} & T_{\mathrm{oi-o}} & G_{\mathrm{ci-o}} \\ Y_{\mathrm{iL-o}} & T_{\mathrm{oL-o}} & G_{\mathrm{cL-o}} \\ G_{\mathrm{io-o}} & -Y_{\mathrm{o-o}} & G_{\mathrm{co-o}} \end{bmatrix} \boldsymbol{u} \tag{2.19}$$

3. INTEGRATING AN ENERGY STORAGE TO A PHOTOVOLTAIC INVERTER

In this chapter, the models presented in Chapter 2 are combined by integrating the EES with the PV inverters using different topologies. The following topologies are considered:

(a) Single-stage PV inverter and EES connected with a bi-directional dc-dc converter at the PV generator terminals

(b) Double-stage PV inverter and EES connected with a bi-directional dc-dc converter at the dc-link

(c) Single-stage PV inverter and EES connected with its own inverter

The topologies are presented in Fig. 3.1. The number of stages in the presented topologies refers to the number of converters and inverters connected in cascade. In the following subsections, these topologies are shortly compared regarding component rating, efficiency, reliability, modularity, costs, and control.

3.1 Component Ratings

In this section, the limits and restrictions related to the component ratings are discussed and analyzed. It is not of concern to take into account issues that are essentially dependent on the chosen application, such as choosing battery capacity or power rating, but rather to focus on the differences directly related to the topologies in order to keep the comparison on a general level.

3.1.1 Limits for the Photovoltaic Module

By using both series and parallel connections, a PV generator can be designed to have the desired nominal voltage and power. However, a PV generator has no natural input voltage range. It is important to ensure that the MPP voltage range of

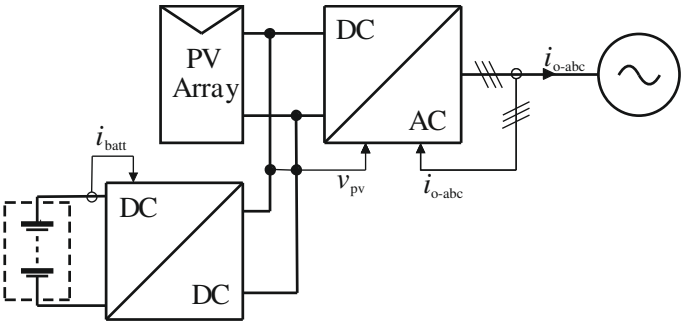

(a) Single-stage PV inverter and EES connected with a bi-directional dc-dc converter at the PV generator terminals

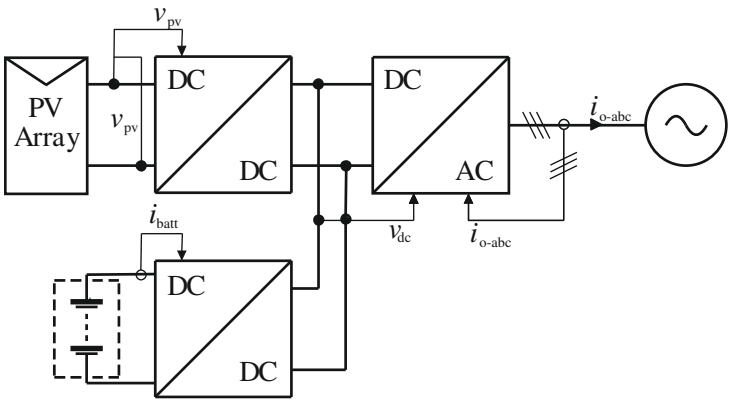

(b) Double-stage PV inverter and EES connected with a bi-directional dc-dc converter at the dc-link

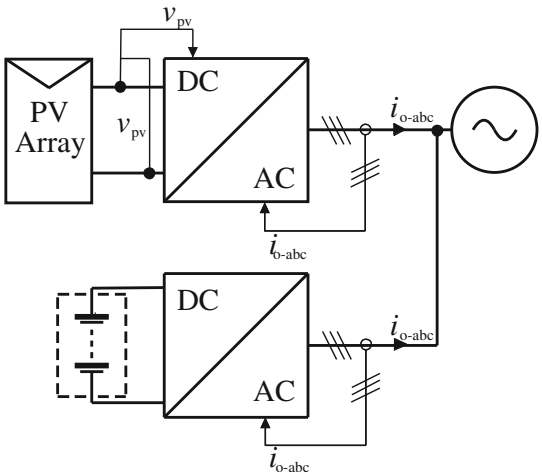

(c) Single-stage PV inverter and EES connected with its own inverter

Figure 3.1 *The different topologies*

a PV array can fit the limited operating voltage range, which can prevent deviation from the MPPs and reduce mismatching losses. The converter or inverter controlling the voltage across the PV modules should have high efficiency over a wide range of input voltage and input power since these variables are defined in very wide ranges as functions of solar irradiance and ambient temperature. Thus, there is a trade-off

regarding the selection of the minimum input voltage, and therefore also the minimum possible MPPT voltage.

Especially for the case of the single-stage inverter, decreasing the minimum possible MPPT voltage results in more energy extracted from the PV panels during low irradiance levels, but a less efficient inverter design [3]. For a single-phase system, the dc-side voltage of the inverter needs to be higher than the peak value of its ac-side voltage and for a three-phase system, higher than the square root of three times the peak value of its ac-side voltage, i.e.

$$\begin{aligned} \text{for single-phase:} \quad & v_{\text{dc}} > v_{\text{ac, peak}} \\ \text{for three-phase:} \quad & v_{\text{dc}} > \sqrt{3}\, v_{\text{ac, peak}} \end{aligned} \tag{3.1}$$

If the dc-side voltage is lower than this limit, the shape of the inverter ac-currents gets distorted due to overmodulation. Similar behavior does not occur when the dc-dc converter is used to control the voltage instead of the inverter. Thus, in order to reach the MPP voltages lower than this limit, the dc-dc converter is required to control the voltage across the PV modules instead of the inverter. Another possibility is to use a diode to bypass the boost converter when the voltage is high enough, as done, for example, in [26]. However, in this case, the diode increases the losses. As a result, the efficiency of the system decreases.

Therefore, during low irradiance levels, the double-stage PV inverter scheme is more efficient, assuming that the increase of MPPT mismatch losses with the single-stage topology would be greater than the losses caused by the additional power conversion stage. However, the best configuration represents an optimal trade-off between the converter losses and MPPT mismatch losses, and is highly dependent on the variation of the solar irradiance levels that are typical for the chosen location.

Since utility-scale PV systems require numerous PV modules, it is possible to connect them in series in order to achieve a high enough voltage level to utilize single-stage PV inverters. According to [5, 16], in order to achieve a high enough input voltage for a single-phase inverter in the European systems (230 V_{rms}) to control the voltage across the PV modules with the inverter instead of the additional dc-dc conversion stage, minimum 16 PV modules in series are required. The minimum required amount of series-connected PV modules of a certain system can be identified by comparing the lowest desired MPP voltage of the modules with the voltage requirement given in Eq. 3.1. For European systems with single-phase inverter, this requirement is 325 V. In Fig. 3.2 are presented the MPP voltage and power as a function of irradiance for different amounts of series-connected PV modules at 25°C.

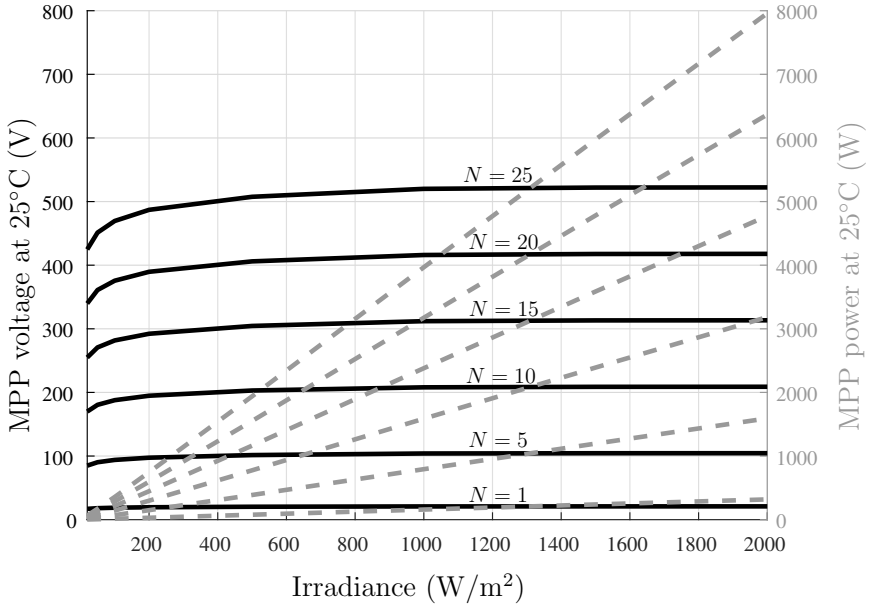

Figure 3.2 *The MPP voltage and the produced power as a function of irradiance for N PV modules connected in series at 25°C*

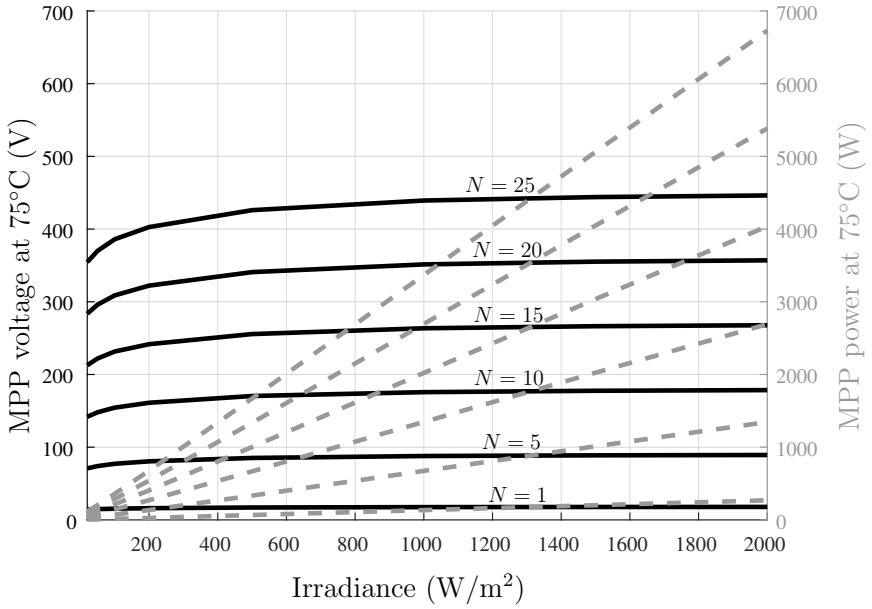

Figure 3.3 *The MPP voltage and the produced power as a function of irradiance for N PV modules connected in series at 75°C*

Based on this figure, 16 PV modules seems feasible when the irradiation stays higher than 500 W/m^2.

However, if the temperature increases, the MPP voltages decrease. In Fig. 3.3 are presented the MPP voltage and power at 75°C. At this high temperatures, 16

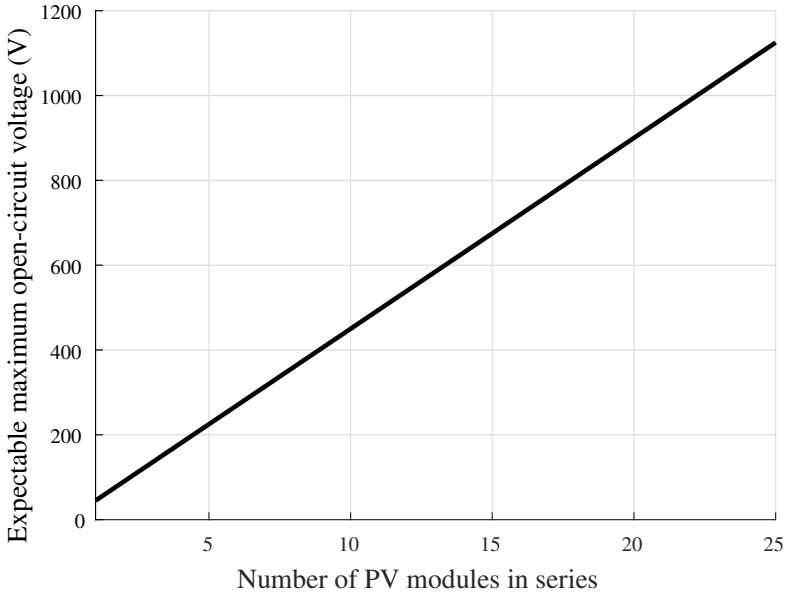

Figure 3.4 *The maximum open-circuit voltage as a function of the number of series-connected PV modules assuming open-circuit voltage of 45 V for one module*

series-connected PV modules does not meet the required minimum voltage but a minimum of 19 modules are needed in order to reach the required voltage around the same minimum irradiance level. Thus, when deciding the operating range of the MPP voltage, it is necessary to take the effect of both the temperature and the irradiance on the MPP voltage into account when choosing the amount of series-connected PV modules.

Fig. 3.4 presents the maximum open-circuit voltage for different amounts of series-connected PV modules. The total open-circuit voltage for 16 PV modules may raise as high as 720 V, which has been too high for MOSFET and IGBT semiconductors in the past, since their normal operating voltage has been as low as 450–510 V [16]. Note, that the operating voltage is typically selected much lower than the breakdown voltage, and this de-rating is based on the need to tolerate transients and to guarantee the long term reliability of the converter [13]. Therefore, in the single-stage PV inverter, multiple semiconductors of this type need to be placed in series in order to reach the required voltage rating. This introduces new problems since it must be guaranteed that these series connected semiconductors function synchronously and switch state at the same time. In order to avoid this and use only single switches in series, semiconductors with higher ratings need to be used or a topology with the additional dc-dc converter and dc-link can be utilized.

However, nowadays in medium power industry applications, such as PV, 600–1700 V

IGBTs are dominant and they typically switch from 10 to 20 kHz [13], thus enabling a more efficient single-stage topology. Furthermore, in the last two decades, newer generations of power semiconductor devices based on wide band-gap materials, such as silicon carbide (SiC) and gallium nitride (GaN), have been developed. The SiC MOSFET switching frequency is significantly higher than 50 kHz and they have already been introduced commercially rating from 600 to 1700 V [13]. Even 15 kV prototypes have been introduced [39]. These new technologies would enable the usage of more efficient single-stage PV inverters.

3.1.2 Limits for the Battery Module

When the battery current is controlled directly by the inverter, the inverter input voltage is defined by the voltage of the battery. Thus, the minimum battery terminal voltage needs to be higher than the limit given in (3.1). The battery terminal voltage and power as a function of the number of series-connected cells are demonstrated in Fig. 3.5 for different kinds of lithium-ion battery systems. The battery is discharged to only 10% charge. Assuming that this is chosen as the lowest limit, the voltage in the figure represents its minimum value, since charging the battery will only increase the voltage and the produced power as well.

For example, in 120 V_{rms} single-phase system, the battery voltage needs to be higher than 170 V. Thus, according to the figure, with C-rate 2, a minimum of 57 series-connected lithium-ion battery cells is required. This can be determined based on the cell voltage at the same charge (3 V), since $170/3 = 57$. With this topology, the power would be around 680 W when only one battery string is set in parallel, as determined by (2.5). The power can be increased by increasing the C-rate or the amount of battery cells.

By adding a dc-dc converter, less series-connected battery cells can be used since the battery voltage can be lower. This may decrease the system cost if the battery would otherwise need to be over-dimensioned in order to reach the required voltage levels without the boosting power stage. In addition, a smaller capacitor is required to regulate the battery voltage when the additional dc-dc converter is utilized. The dc-link is more preferable location for the capacitor since the voltage is higher and a large fluctuation can be allowed without compromising the utilization factor [16].

Moreover, in the single-stage connection of the EES, the inverter input voltage is directly defined by the voltage of the EES. Since battery voltages vary greatly depending on the SoC, it introduces variation to the inverter input voltage. Therefore,

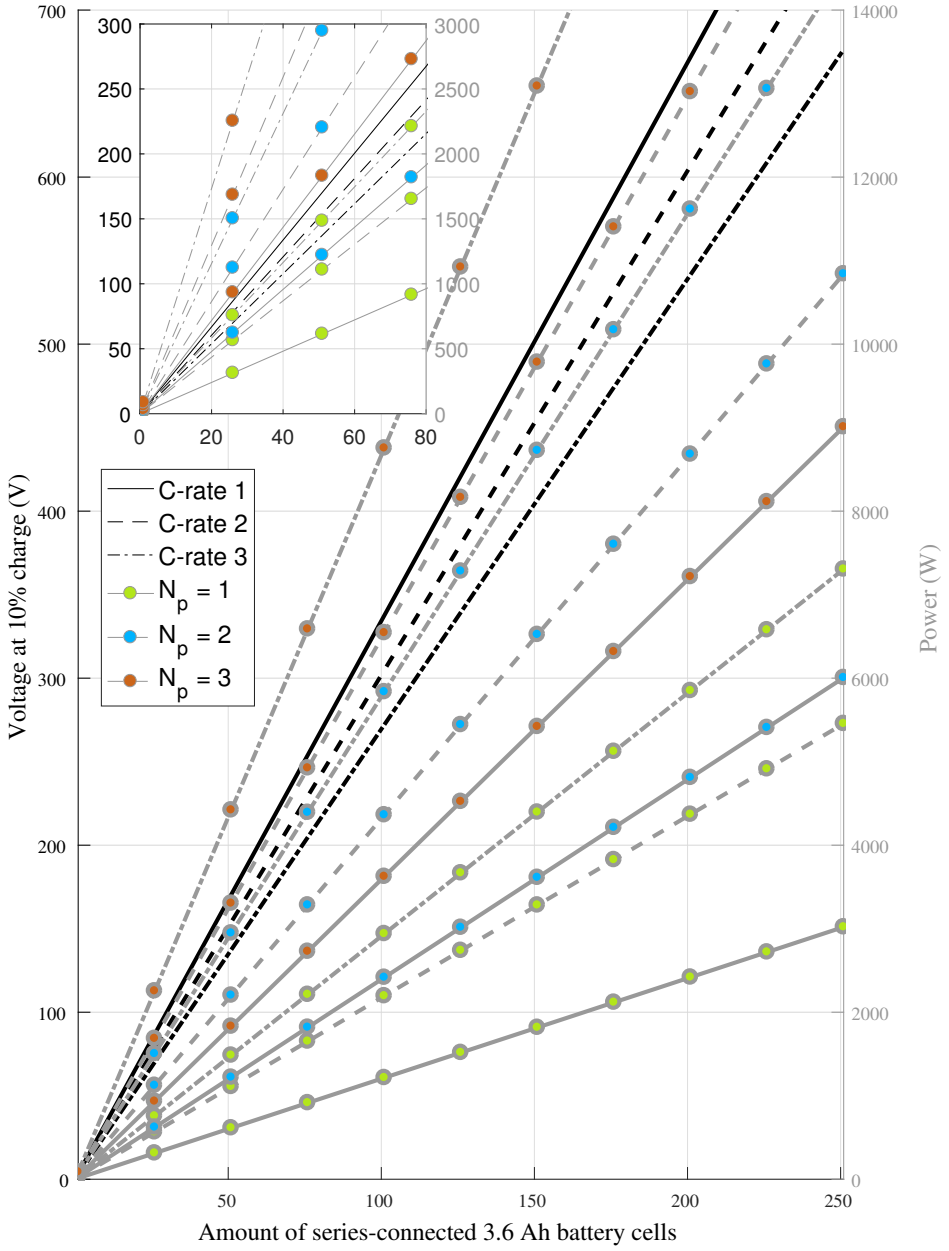

Figure 3.5 *The battery terminal voltages and powers at full charge (90%) with different C-rates and numbers of parallel-connected cells. The lines with green markers have 1 cell in parallel, blue markers 2 cells, and orange markers 3 cells. The lines with solid line-style are with C-rate 1, dashed line-style C-rate 2, and dash-dot line-style C-rate 3*

these inverters are required to accommodate the entire range of operating voltage and their design in terms of semiconductor selection and operating points is not optimized in the same way as with the double-stage topology where the dc-link voltage is set constant [40]. Thus, especially if the battery voltage range would be required to be impractically wide and/or the grid current THD to be low, a bi-directional dc-dc converter is recommended in order to meet these requirements.

Furthermore, if the additional dc-dc converters are included to regulate the batteries, there is no apparent difference in terms of battery management and safety when using different grid-tied converters. In addition, according to [40], if the additional dc-dc converter is left out, low-order harmonics, occurring for example under grid faults, may decrease the battery lifetime and cause safety concerns. Certain dc-dc topologies may also serve as protective and current limiting devices, eliminating the need for costly dc breakers [40].

A typical operating condition of storage batteries requires to deliver and absorb small currents in large intervals of time. However, as listed in Chapter 2, new methods to utilize grid-connected EESs require the EES to be able to manage large currents in short intervals of time. One of the main concerns has been how the fast and short cycling (micro-cycling) affects the lifetime of the batteries. Thus, in many applications, super-capacitors are proposed to be used in addition to batteries due to their higher power density, as in [12]. However, in [7] it was shown that fast and short cycling of lithium-ion batteries did not show a substantially altered capacity fade during the execution of hundreds of thousands of micro-cycles. Thus, the usage of lithium batteries without the super-capacitors can be considered reasonable for these applications.

The capacity of the EES is not analyzed further since it rather depends on the chosen application than the chosen topology. For further reading, the required capacity of an EES in order to provide constant power production to the grid from a PV plant has been studied, for example, in [4].

3.2 Efficiency and Losses

From efficiency point of view, the total loss in a single-stage PV inverter is slightly smaller than that in a two-stage PV inverter [43]. The additional dc-dc converters produce power losses, which to some extent explains why most industrial solutions currently do not include the additional dc-dc stage. However, regarding the total energy efficiency, the mismatching losses are most of the times more significant than the switching losses. Especially in partial shading conditions, the mismatching losses may more than compensate the switching losses.

During low irradiance levels, the double-stage PV inverter scheme is more efficient than the single-stage, assuming that the increase of mismatching losses with the single-stage topology would be greater than the losses caused by the additional power conversion stage. However, since the dc-dc conversion losses do not take place in the single-stage topology, the total efficiency of the system is higher. This

may be of utmost importance especially in utility-scale systems since even a small difference in the efficiency can indicate large power losses. However, in order to calculate the overall efficiency, the efficiency of the topology at each operating point and the amount of time spent at that operating point should be considered. As discussed in [43], if the operating voltage range of a single-stage system is properly limited, its overall efficiency will be higher than that of a two-stage system.

As discussed in Section 2.1, long series connections of PV modules are the ones most severely affected by partial shading conditions. In addition to mismatching losses caused by too low or high irradiance levels, the additional dc-dc stage enables the use of less series-connected PV modules, which is beneficial in partial shading conditions, as discussed in Section 2.1. This topology decreases the mismatching losses caused by partial shading conditions etc. Therefore, in locations where partial shading situations can be expected to occur most of the time, the dc-dc converter is necessary to mitigate the mismatching losses.

As will be discussed more in detail in Section 3.5.1, by utilizing the additional dc-dc converter to control the voltage across the PV generator, a faster MPP control can be achieved in comparison with the single-stage inverter. Thus, the MPPT function can update its tracking command immediately so that the effect of fast irradiance variation can be ignored [43]. This also decreases the mismatch losses and improves the total efficiency.

The topology, in which the PV modules and the batteries are integrated with their own separated inverters, requires advanced and expensive high voltage semiconductors, as discussed in Section 3.1. However, less power conversion stages are required, which is an advantage from the efficiency point of view.

3.3 Modularity

In the future, standalone micro-grids, powered by renewable energies like solar and wind turbines, will play a crucial role in generating electricity for local communities. The grid-forming topology can be used, for example, in remote locations where the traditional utility power grid is inaccessible. As discussed in Chapter 2, in order to utilize grid-forming mode instead of just grid-feeding mode and at the same time to control the voltage across the PV modules to correspond the MPP voltage, a dc-dc converter is required. Due to the intermittent nature of solar power, it is necessary to utilize a storage, such as a battery, as a back-up to complement the PV in order to maintain the micro-grid voltage and frequency during lower irradiance levels.

Furthermore, having an inverter with both grid-feeding and grid-forming mode is beneficial, since the possibility for grid-forming mode can be used as a back-up in case of grid failures. When the inverter is isolated from the utility grid, it can be used as an uninterrupted power supply (UPS) to feed critical loads.

In some applications, a local dc-grid may be beneficial. By utilizing a local dc-grid, power losses from the inverter can be eliminated. The dc-link offers a good interface for this function. The dc-grid can be utilized to supply local dc-loads, such as household electrical equipment.

During the lifetime of the PV generator, the PV modules may need to be changed due to a fault etc. When considering the installation process, the single-stage PV inverter design may be required to be individual for each separate PV system installation due to the different environment etc., and thus a less flexible design is achieved in comparison with the topology in which the dc-dc converter is utilized [5].

Another important factor in the design is the possibility to enlarge the system. The topology, in which the PV modules and the batteries are integrated with their own inverters, offers the possibility of an easy enlargement of the system due to the modular structure [16].

However, also the dc-link offers a good interface for the enlargement of the system. By utilizing the dc-link, numerous PV modules and batteries can be interfaced with their own dc-dc converters to the common dc-ac inverter. Thus, the operator can start the PV power plant with fewer modules and further enlargements are easily achievable since a new dc-dc converter with the new PV modules can be plugged into the existing platform [5]. Therefore, enlargement of the system is easy and a highly flexible design can be achieved. This topology may be considered the most optimized one for systems with several PV strings [16].

In addition, when considering the EES enlargement, a larger capacity can be easily achieved by connecting several battery strings in parallel to a common dc bus by bi-directional dc-dc converters. Thus, the topology with the dc-link allows easy enlargement of the EES, too.

3.4 Cost and Profit

From the operator's point of view, the inverter must be cost-efficient. Nowadays, improvements in PV inverter systems are mainly linked to a reduction of overall system costs, since their efficiency is above 98 % in all cases and thus not the main focus of development anymore [32].

A single-stage system has the merits of saving components and reducing cost, since the additional dc-dc converter increases the system cost. However, the single-stage system may be less energy efficient due to the PV mismatch losses, as discussed in Section 3.2. Thus, the efficiency can compensate the initial costs in some applications, especially under partial shading conditions.

As discussed in [31], the profitability of connecting an EES to PV plants depends on various parameters, but the key contributor is the revenue from selling the stored electricity. Since the profit from selling the electricity depends on the electricity markets, the policies, and the environment, it is necessary to consider each situation individually. The profitability of the EES is less sensitive to the battery key-figures, such as the number of life-cycles and the battery price [31]. Thus, in order to enable optimized revenue, the electricity markets should reward the providers of EESs. In addition, when calculating the costs of the EES, it is necessary to take into account also the maintenance and replacement costs which depend on the chosen battery type [15].

As discussed in Section 3.1, advanced semiconductors, such as SiC MOSFETs, are required if a single-stage inverter is utilized. However, the relatively higher cost of SiC devices is still a concern [13]. On the other hand, the operational cost reduction gained from efficiency improvements could justify the higher cost [6]. In addition, the faster switching reduces the required filter size and cost. Compensating savings may come from smaller passive components, lower cooling requirements, and a higher absolute power rating [13]. For instance, it is demonstrated in [32], that the cost of a 17 kW solar inverter could be reduced by 20 % with SiC JFETs and SiC diodes. According to [13], due to their potentials to improve the power efficiency while reducing the system cost, PV inverters could be the first major insertion point for SiC power devices.

3.5 Converter Control

In this chapter, the differences between the controlling strategies of the different topologies presented in Section 3 are analyzed and compared. The controlling schemes of the bi-directional dc-dc converter, the boost converter and the inverter are discussed and analyzed.

3.5.1 PV Inverter Control

The PV inverters have normally two main tasks: to ensure that the PV modules are operated at the MPP and to inject a sinusoidal current to the grid. In order to achieve this, a cascaded control scheme is used to regulate the dc-link voltage and the output current. The outer input-voltage control-loop provides the current reference d-component to the inner output-current control-loop. The output-current q-component reference is usually set to a value (0) which guarantees unity power factor.

The input voltage reference depends on the chosen topology. In general, the control of a single stage solution is definitely simpler than the double stage solution as only one stage has to be controlled [28]. If a double-stage inverter is used, the inverter input voltage reference is the dc-link voltage, which is kept as a constant, and the dc-dc converter is used to perform the MPPT algorithm in order to maximize the energy produced by the PV generator. Thus, the MPPT algorithm can be used to control the duty cycle directly.

In the case of a single-stage inverter, the inverter input-voltage reference is determined by the MPPT algorithm. Consequently, the input voltage reference can vary rapidly. In this topology, due to the cascaded control scheme, the MPPT can not be as fast as when the double-stage inverter is utilized. The MPPT control is limited by the cross-over frequency of the voltage control. This leads to additional mismatching losses compared to the double-stage inverter since the PV generator does not operate at MPP as accurately. The input-voltage control should be designed so that the bandwidth exceeds the MPPT-algorithm execution frequency.

In case the PV inverter would be required to function also in grid-forming mode, the inverter would need to control both the output current and voltage. Thus, the input voltage would not be controlled by the inverter, and a double-stage topology would be necessary in order to perform the MPPT. If EES is connected to the dc-link of the inverter, it can be used to verify the location of the MPP and to support the recovery of the system from instability. These functions may be necessary especially in grid-forming mode.

3.5.2 Battery Control

The battery current is controlled by either a bi-directional converter or a VSI in order to charge and discharge the battery according to the requirements of the chosen application, as discussed in Chapter 2. The reference current may, for example, be

determined according to the measured PV power in order to limit the rate of change of power fed to the grid. If the goal is to feed constant power to the grid, Eq. 3.2 may be used to determine the current reference.

$$i^*_{\text{batt}} = (P^*_{\text{grid}} - P_{\text{pv}})/v_{\text{batt}}. \tag{3.2}$$

Batteries are very sensitive to over- and undercharge. Extended periods of undercharging lead to sulphation and stratification, whereas overcharging causes gassing and grid corrosion. These chemical changes shorten the battery lifetime. Especially in PV systems, the batteries are subject to performance losses that are caused by the limited availability of energy to recharge the battery [2]. Hence, it is necessary to limit the SoC and to keep it within safe limits. This should be taken into account when designing the control in order to keep the system stable in all conditions and to increase the battery lifetime. For instance, in [14], the SoC which should be reached at the end of the day is chosen based on the weather predictions of the next day. This method guarantees the capability and lifetime of the battery and also minimizes operation cost since the battery can be charged during low electricity price.

Various charging methods have been designed for different applications and battery types. In PV systems, it is necessary that the effectiveness of maintaining the battery at a high SoC is guaranteed, thus increasing the lifetime of the battery. Therefore, the best charging method is one that returns the most charge to the battery in the quickest time without causing a significant rise in the battery temperature [2].

When the PV system under MPPT control is integrated with the EES, the power balance in the dc system and the battery reliability become an issue due to the intermittent behavior of the PV system. If not taken properly into account, excessive power from PV leads to over voltage in the dc bus and in cloudy conditions the dc bus becomes unstable [36]. In order to prevent both stability issues, the power balance control needs to be taken into account.

Therefore, it may not be possible to utilize MPPT at all times, such as when the battery is full and the power from PV is needlessly high. In this case, the PV power needs to be limited with a power limiting algorithm instead of utilizing MPPT and the battery needs to be, for example, disconnected from the system or discharged in another way.

In case the PV power is too low for the application requirements and the battery

SoC is at its lower limit, a back-up battery could be one solution. The situation is naturally an implication that the battery size should be increased or the discharging algorithm changed in order to avoid the problems in the future.

In case of grid-forming mode of the inverter, a bi-directional dc-dc converter is necessary in order to control the battery current, since the inverter cannot be used to perform that functionality as was possible with the grid-feeding inverter. Thus, the single-stage topology is not suitable for this function.

4. PERFORMANCE EVALUATION

Simulations are conducted with MATLAB Simulink software in order to demonstrate the power balance control and the differences between the topologies stated in the earlier chapters. In addition, real-time simulations are conducted with the BoomBox control platform by Imperix, combined with the real-time emulator for hardware-in-the-loop (HIL) simulation by Typhoon-HIL.The set up consists of a Typhoon HIL 402, which is in charge of high-fidelity real-time simulation, interfaced with Imperix's Boombox, which is in charge of running the control code. This set-up enables the implementation of the controllers to be directly confronted to almost real conditions allowing to foresee most of control related issues before the usage of the real implementation. A figure of the set-up is given in Appendix A. The simulation model and the results are presented and discussed in this chapter.

4.1 Parameters and Controller Tuning

The parameters for the modeling of the PV generator are presented in Table 4.1. The PV model is based on the one diode model [23] as discussed in Chapter 2. In Fig. 4.1 are shown the voltage and current characteristics of one PV module under standard test conditions.

The parameters for modeling of the battery are presented in Table 4.2. The battery current limits are calculated based on the C-rate according to (2.5). The amount of battery cells is chosen based on the required voltage level. If the battery is directly connected to the inverter, 100 modules are required.

The topology of the double-stage PV inverter where the EES is connected with a bi-directional dc-dc converter at the dc-link is presented in Fig. 4.2. In Fig. 4.3 the topology of the single-stage PV inverter where the EES is connected with a bi-directional dc-dc converter at the PV generator terminals is presented.

The values related to the grid, the converters, and the LCL-type filter are presented in Table 4.3. The grid values are chosen according to the US standards and the filter values are chosen according to [19, 41] so that the inverter output current ripple is

Table 4.1 *PV module parameters*

Number of series connected PV modules	N_{series}
Short-circuit current (in STC)	8.1 A
Open-circuit voltage (in STC)	$25 \cdot N_{\text{series}}$ V
Temperature T	298.15 K
Irradiance (in STC)	1000 W/m^2
Series resistance R_{s}	$1.37 \cdot N_{\text{series}}$ Ω
Shunt resistance R_{sh}	$589.94 \cdot N_{\text{series}}$ Ω
Temp coeff of I_{sc}	$0.0047 \cdot N_{\text{series}}$
Temp coeff of U_{oc}	$-0.12 \cdot N_{\text{series}}$
Boltzmann constant k	$1.38 \cdot 10^{-23}$
Elementary charge q	$1.602 \cdot 10^{-19}$ C
Ideality factor A	1.30

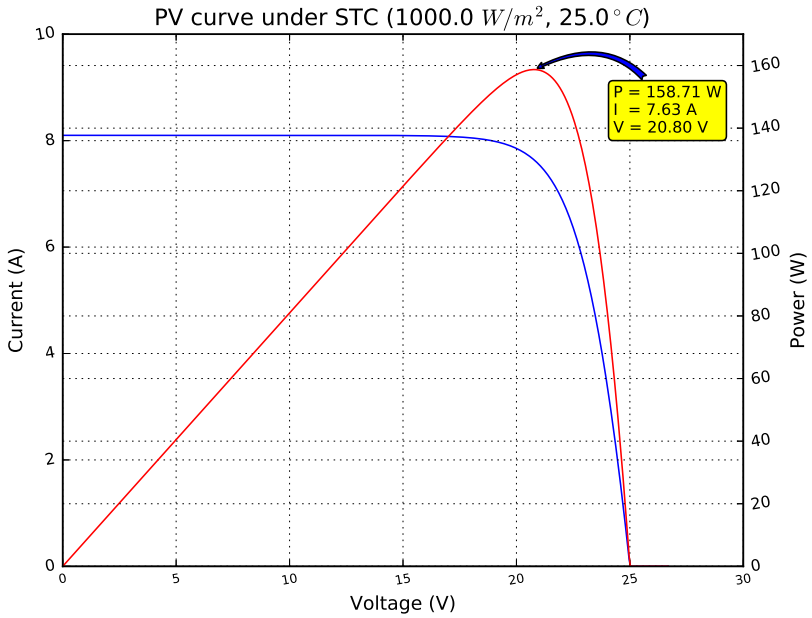

Figure 4.1 *Current, voltage, and power characteristics of the PV module under standard test conditions*

less than 20% and the grid-side inductor current ripple less than 2%. As done in [19], the damping value is chosen one-third of the filter capacitor at the resonant frequency, i.e., 0.6 Ω. The inverter output current q-component I_{Lq} is here controlled to 0 which results in unity power factor for the inverter-side current.

As discussed in [25], the PV voltage control needs to be designed so that the bandwidth exceeds the MPPT-algorithm execution frequency. A crossover frequency of two hundredth of the switching frequency (i.e. 400 Hz) is chosen and the following

Table 4.2 *Battery parameters*

Cell capacity Q	3600 mAh
Initial Charge	$0.6 \cdot Q$ mAh
Number of series-connected cells N_s	50 or 100
Number of parallel-connected cells N_p	1
Exponential zone time constant inverse B	3.5294/3600 Ah^{-1}
Exponential zone amplitude A	0.468 V
Polarization voltage K	8.7662 mV
Internal resistance R_int	90 mΩ
Battery constant voltage E_0	3.7348 V
C-rate C_r	2

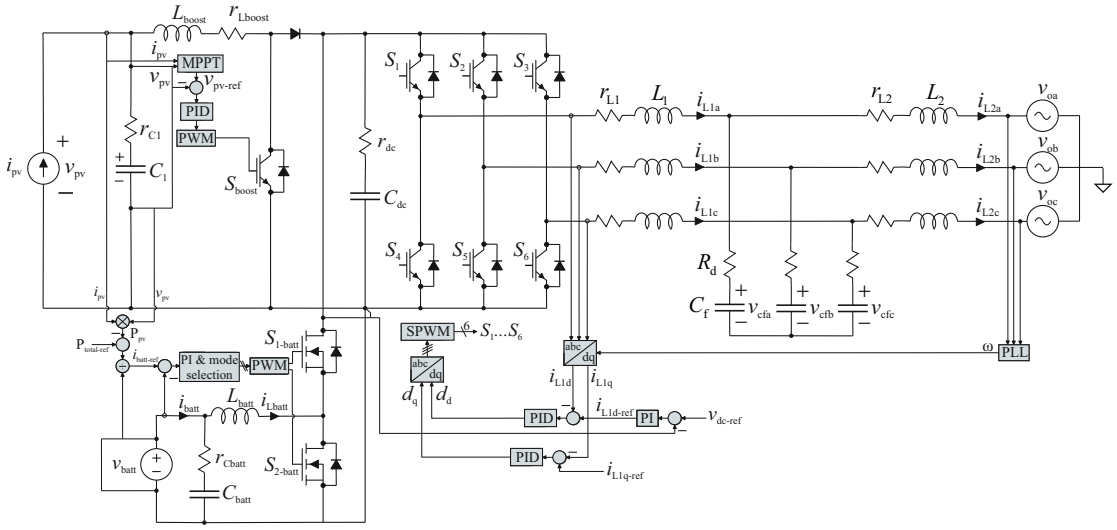

Figure 4.2 *Double-stage PV inverter and EES connected with a bi-directional dc-dc converter at the dc-link*

controller transfer function is used.

$$G_{\mathrm{c-boost}} = K_{\mathrm{boost}} \frac{\left(\dfrac{\mathrm{s}}{\omega_{\mathrm{z-boost}}} + 1\right)^2}{\mathrm{s}\left(\dfrac{\mathrm{s}}{\omega_{\mathrm{p-boost}}} + 1\right)}. \tag{4.1}$$

The boost converter is tuned as follows using the loop shaping technique. The open-loop control to input-voltage transfer function $G_{\mathrm{ci-o}}$ attained from (2.15) with a delay of 1.5 times the switching period is shown in Fig. 4.4 as a black line. The

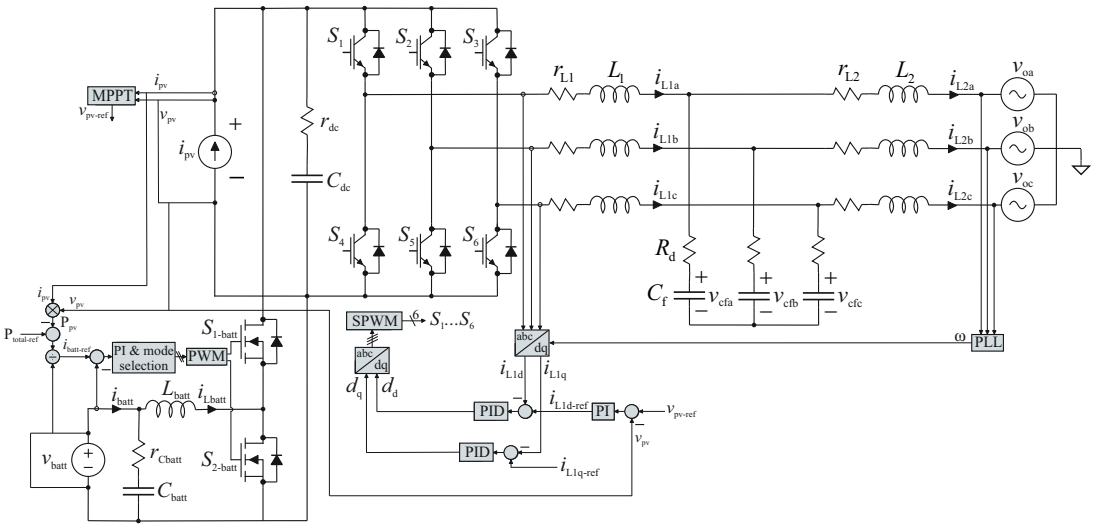

Figure 4.3 *Single-stage PV inverter and EES connected with a bi-directional dc-dc converter at the PV generator terminals*

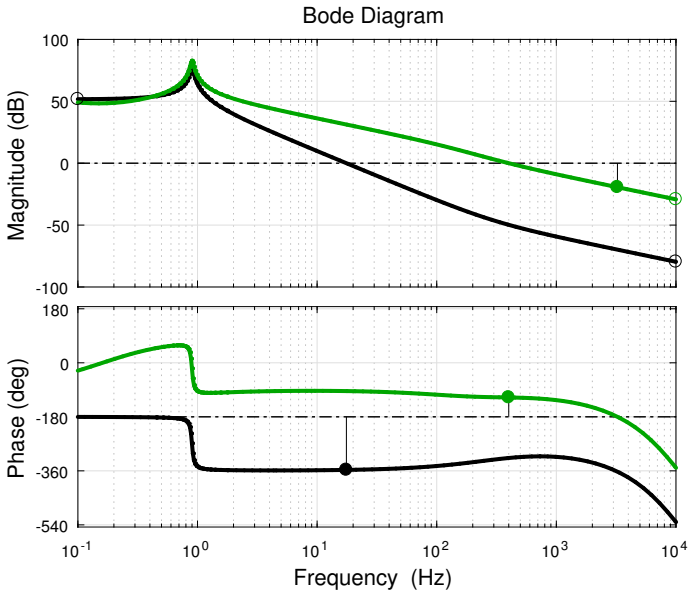

Figure 4.4 *The boost converter control to input-voltage transfer function $G_{\mathrm{ci-o}}$ depicted with the black line and the controller loop gain $G_{\mathrm{ci-o}}G_{\mathrm{c-boost}}$ with the green line*

system with a delay is approximated using a 3rd order Pade approximation. The dc-gain of $G_{\mathrm{ci-o}}$ is negative. Thus, a negative controller gain is required in order to ensure stable operation. The controller zeros and poles are chosen so that a phase margin of 65° is reached. The chosen controller parameters are given in Table 4.4 and the controller loop gain is shown in Fig. 4.4 as a green line.

Table 4.3 *Grid, converter, and LCL-type filter parameters.*

$V_{\mathrm{o-invrms}}$	120 V	$V_{\mathrm{od-inv}}$	$\sqrt{2}V_{\mathrm{o-rms}}$ V
f_{grid}	60 Hz	ω_{s}	$2\pi f_{grid}$ rad/s
I_{Ld}	10 A	I_{Lq}	0 A
Double-stage PV		Single-stage PV	
$V_{\mathrm{in-inv}}$	380 V (350–410 V)	$V_{\mathrm{in-inv}}$	675 V (350–900 V)
V_{pv}	10–350 V	V_{pv}	350–900 V
C_{batt}	1 mF	C_{batt}	1 mF
r_{Cbatt}	90 mΩ	r_{Cbatt}	90 mΩ
L_{batt}	100 mH	L_{batt}	100 mH
L_1	3.25 mH	L_1	8 mH
r_{L1}	22 mΩ	r_{L1}	22 mΩ
L_2	115 µH	L_2	115 µH
r_{L2}	65 mΩ	r_{L2}	65 mΩ
C_{f}	16 µF	C_{f}	16 µF
R_{d}	0.6 Ω	R_{d}	0.6 Ω
f_{sw}	20 kHz	f_{sw}	20 kHz
C_{dc}	150 µF	C_{dc}	2.9 mF
r_{Cdc}	10 mΩ	r_{Cdc}	10 mΩ
L_{boost}	580 mH		
r_{Lboost}	10 mΩ		
C_1	54 mF		
r_{C1}	10 mΩ		

The transfer function of the bidirectional converter controller (battery current controller) is chosen as

$$G_{\mathrm{c-ibatt}} = K_{\mathrm{batt}} \frac{\left(\frac{\mathrm{s}}{\omega_{\mathrm{z-batt}}} + 1\right)}{\mathrm{s}}. \tag{4.2}$$

The open-loop control to inductor current transfer function $G_{\mathrm{ci-o}}$ is shown in Fig. 4.5 as a black line. The controller zero is chosen so that the phase margin given in Table 4.4 is met. The chosen parameters are given in Table 4.4 and the controller loop gain is shown in Fig. 4.5 as a green line.

As discussed in Chapter 2, due to the cascaded control method of the output current d-component and the input voltage, the inverter is able to control the active power, the reactive power, and the dc-link voltage (or the PV voltage, depending on the chosen topology). The controlling method is presented in Fig. 2.10. The open-loop

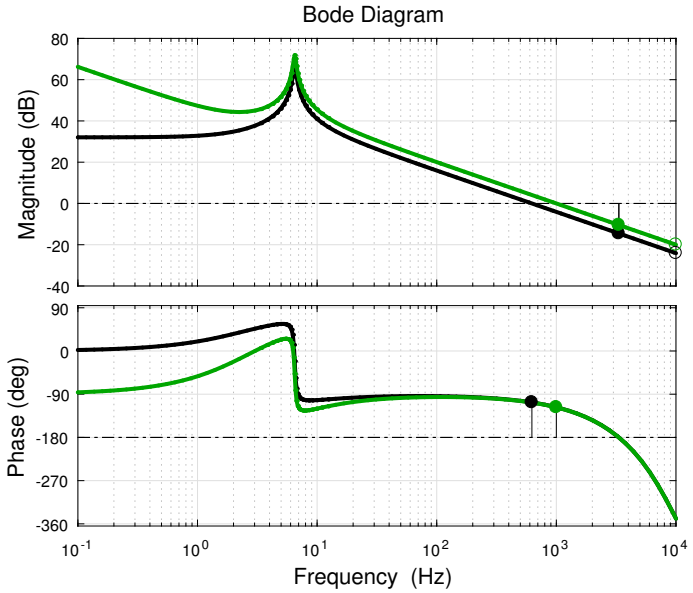

Figure 4.5 *The bidirectional converter controller (battery current controller) control to input-voltage transfer function $G_{\mathrm{ci-o}}$ depicted with the black line and the controller loop gain $G_{\mathrm{ci-o}}G_{\mathrm{c-batt}}$ with the green line*

control to inverter current d component transfer function $G_{\mathrm{cLd-o}}$, the open-loop control to inverter current q component transfer function $G_{\mathrm{cLq-o}}$, and the open-loop control to input voltage transfer function $G_{\mathrm{cid-o}}$, are shown in Fig. 4.6 for the single-stage PV inverter topology and in Fig. 4.7 for the double-stage PV inverter topology.

The input voltage and output current d-component are controlled in a cascaded manner. According to Fig. 2.10(a), by ignoring the sensing transfer functions, the loop gain for the input voltage controller tuning can be given as

$$L_{\mathrm{v}} = \frac{L_{\mathrm{d}}}{1 + L_{\mathrm{d}}} \frac{G_{\mathrm{cid-o}}}{G_{\mathrm{cLd-o}}}, \tag{4.3}$$

where $L_{\mathrm{d}} = G_{\mathrm{cd}}G_{\mathrm{cLd-o}}$ (i.e. the loop gain of the inner controller loop). The transfer functions of the chosen current controllers G_{cd} and G_{cq} are of the form

$$G_{\mathrm{c}} = K \frac{\left(\frac{\mathrm{s}}{\omega_{\mathrm{z}}} + 1\right)}{\mathrm{s}\left(\frac{\mathrm{s}}{\omega_{\mathrm{p}}} + 1\right)}. \tag{4.4}$$

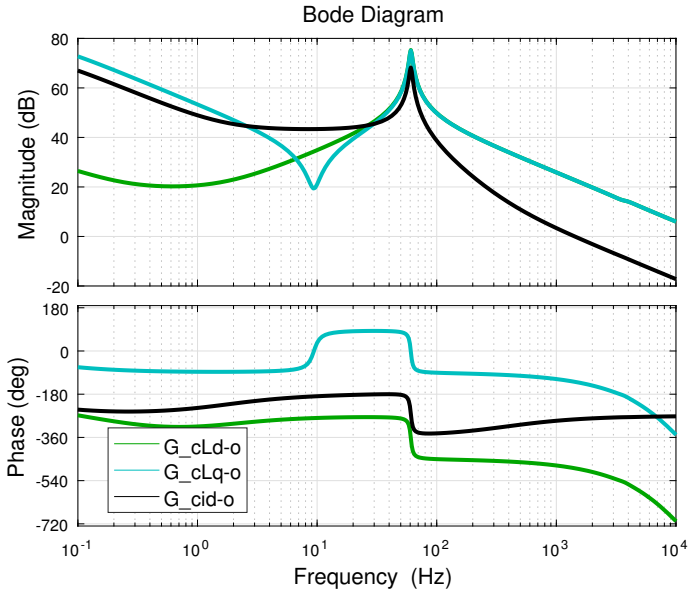

Figure 4.6 *The control to inverter current transfer functions $G_{\mathrm{cLd-o}}$ and $G_{\mathrm{cLq-o}}$ and the control to input voltage transfer function, $G_{\mathrm{cid-o}}$ are depicted as green, blue, and black line, respectively, for the single-stage topology*

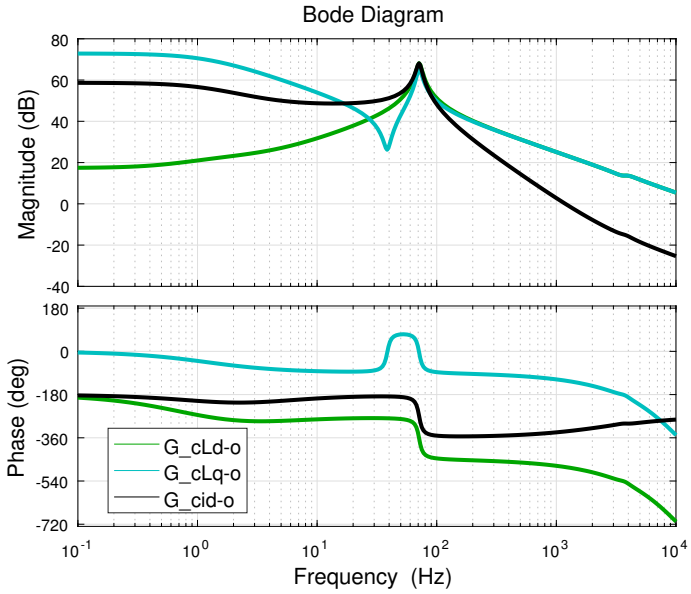

Figure 4.7 *The control to inverter current transfer functions $G_{\mathrm{cLd-o}}$ and $G_{\mathrm{cLq-o}}$ and the control to input voltage transfer function, $G_{\mathrm{cid-o}}$ are depicted as green, blue, and black line, respectively, for the double-stage topology*

and the transfer function of the voltage controller of the form

$$G_{\mathrm{c}} = K\frac{\left(\frac{\mathrm{s}}{\omega_{\mathrm{z}}}+1\right)}{\mathrm{s}}. \tag{4.5}$$

The controller poles and zeros are chosen so that the phase margins given in Table 4.4 are satisfied. The inner loop L_{d} is stabilized with the outer loop control (G_{cv}). The chosen parameters are given in Table 4.4 for both the single-stage and the double-stage PV inverter and the controller loop gains are shown in Fig. 4.8 for the single-stage PV inverter topology and in Fig. 4.9 for the double-stage PV inverter topology. The inverter output current is limited to 20 A since larger currents would trip the protection in a real system.

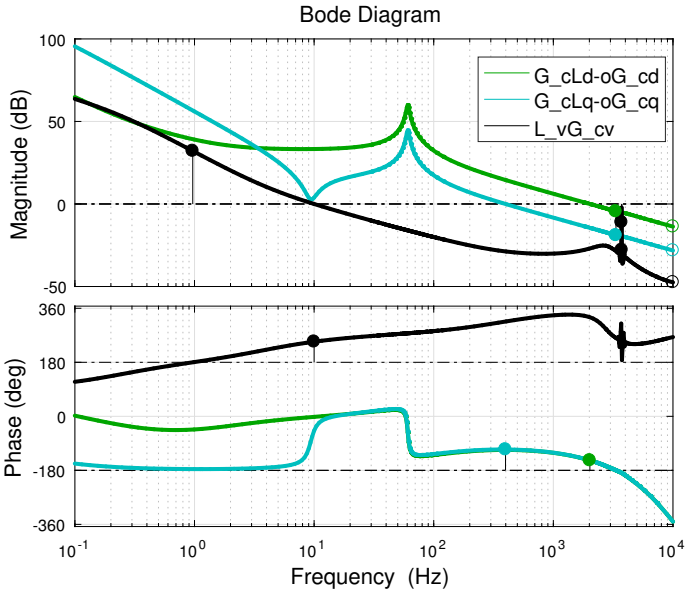

Figure 4.8 *The inverter current controller loop gains $G_{\mathrm{cLd-o}}G_{\mathrm{c-d}}$ and $G_{\mathrm{cLq-o}}G_{\mathrm{c-q}}$ and the input-voltage controller loop gain $L_{\mathrm{v}}G_{\mathrm{c-v}}$ are depicted as green, blue, and black line, respectively, for the single-stage topology*

4.2 Experiments

First, the power balance control is demonstrated using the aforementioned parameters for the double-stage PV inverter topology. The irradiance level is increased stepwisely according to Fig. 4.10(a). The corresponding power produced by 2 PV modules functioning under MPPT control is shown in Fig. 4.10(b) with the blue line. In order to use the battery to compensate the fluctuations in the PV power and to feed a constant power to the grid, the battery current reference is calculated according to (3.2). The produced battery power is shown in Fig. 4.10(b) with the green line and the orange line dictates the sum of the PV power and the battery power. The grid power reference is set to 300 W.

Next, the power balance control is demonstrated using real irradiance measurement data shown in Fig. 4.11(a). The data is measured from solar panels at Tampere

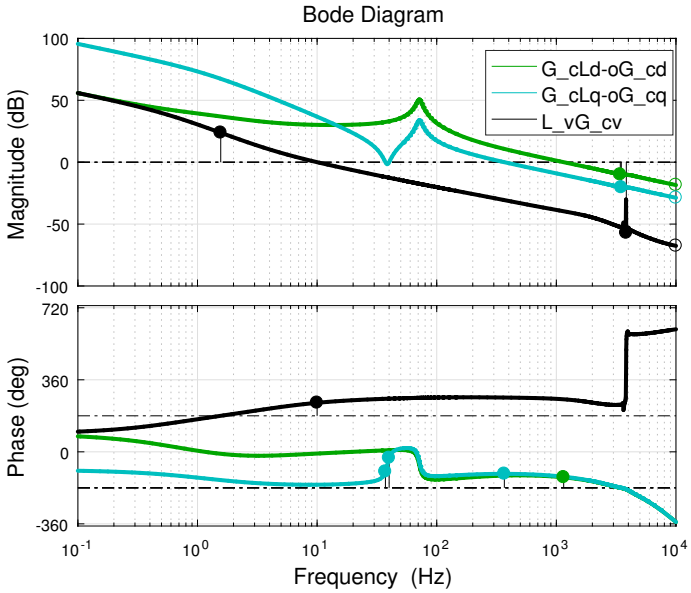

Figure 4.9 *The inverter current controller loop gains $G_{\mathrm{cLd-o}}G_{\mathrm{c-d}}$ and $G_{\mathrm{cLq-o}}G_{\mathrm{c-q}}$ and the input-voltage controller loop gain $L_{\mathrm{v}}G_{\mathrm{c-v}}$ are depicted as green, blue, and black line, respectively, for the double-stage topology*

University of Technology (TUT) Solar Photovoltaic Power Station Research Plant located in Finland on a half-cloudy summer day, 12th July 2016. As can be seen, the irradiance has a highly fluctuating behavior. The corresponding power produced by 8 PV modules functioning under MPPT control is shown in Fig. 4.11(b) with the blue line. In order to use the battery to compensate the fluctuations in the PV power and to feed a constant power to the grid, the battery current reference is again calculated according to (3.2). The battery current is shown in Fig. 4.11(c) and the power it produces in Fig. 4.11(b) with the green line. The sum of the battery and the PV power is shown in Fig. 4.11(b) with the orange line. The grid power reference is set to 2550 W. However, due to the losses within the system (such as the switching losses) and the open-loop structure of the power balance control, the produced power is noticeably smaller, around 2500 W. The currents fed to the grid are presented in Fig. 4.12(a) and their harmonic spectrum is shown in Fig. 4.12(b). The THD is 3.6%.

As discussed in Chapter 3, it is important to limit the battery charge since batteries are very sensitive to over- and undercharge. Problems occur, for example, when the PV modules are producing excess power and the battery charge is too high for the battery to be charged. In this case, the battery needs to be disabled or discharged enough to be used again for storing the excess energy. In both the cases, MPPT cannot be utilized, but instead a power limiting algorithm can be used.

Table 4.4 *Controller parameters for the single-stage PV inverter and EES converter at the PV terminals.*

Single-stage PV				**Double-stage PV**			
Battery converter				Battery converter			
f_{cross}	1 kHz	PM	65°	f_{cross}	1 kHz	PM	65°
$\omega_{\text{z-batt}}$	20 rad/s	K_{batt}	32	$\omega_{\text{z-batt}}$	20 rad/s	K_{batt}	32
MPPT				MPPT			
f_{mppt}	2.5 Hz	Δ_{MPPT}	0.3 V	f_{mppt}	2.5 Hz	Δ_{MPPT}	0.3 V
Inverter inner loop control (i_{d})				Inverter inner loop control (i_{d})			
f_{cross}	2 kHz	PM	35°	f_{cross}	2 kHz	PM	35°
$\omega_{\text{z-od}}$	500 rad/s	$\omega_{\text{p-od}}$	250 krad/s	$\omega_{\text{z-od}}$	820 rad/s	$\omega_{\text{p-od}}$	250 krad/s
K_{od}	52			K_{od}	37		
Inverter outer loop control (v_{pv})				Inverter outer loop control (v_{dc})			
f_{cross}	10 Hz	PM	68°	f_{cross}	25 Hz	PM	68°
$\omega_{\text{z-v}}$	25 rad/s	K_{v}	-9	$\omega_{\text{z-v}}$	63 rad/s	K_{v}	-21
Inverter current q-component control (i_{q})				Inverter current q-component control (i_{q})			
f_{cross}	400 Hz	PM	70°	f_{cross}	400 Hz	PM	70°
$\omega_{\text{z-oq}}$	440 rad/s	$\omega_{\text{p-oq}}$	250 krad/s	$\omega_{\text{z-oq}}$	440 rad/s	$\omega_{\text{p-oq}}$	250 krad/s
K_{oq}	8.6			K_{oq}	3.7		
				Boost converter			
				f_{cross}	400 Hz	PM	65°
				$\omega_{\text{z-boost}}$	1 rad/s	$\omega_{\text{p-boost}}$	1 krad/s
				K_{boost}	-0.33		

This is demonstrated in Fig. 4.13 with power balance control. Double-stage PV inverter topology is used and the grid reference is set to 500 W, shown in the figure with the orange line. The battery power is shown with the green line and the PV power with the blue line. The battery is set to discharge when its charge becomes higher than 90% and the PV modules are set to produce reduced power. After the battery is discharged enough, it is used again to store the excess energy. In order to avoid situations where the battery charge would exceed its limit, its capacity should be chosen based on the application and irradiation levels and the charging and discharging algorithms should be chosen in a way that results as small changes to the charge level as feasible. For example, in certain applications, such as in ramp-rate control, it would be beneficial to charge and discharge the battery so that the charge would have only minor changes over time.

As discussed in the tuning of the converters, it is advantageous to have as high

bandwidth for the PV voltage controller as possible. This enables faster tracking and thus also the MPPT execution frequency can be increased. This results in higher efficiency. The difference in the controllers is demonstrated in Fig. 4.14 with a 5 Hz cross-over frequency and in Fig. 4.15 with a 25 Hz cross-over frequency. It can be noticed from the figures that the controller with the higher cross-over frequency (higher bandwidth) follows the reference faster, as expected.

As discussed in Chapter 3, the input voltage of the inverter cannot be lower than given in (3.1). In the single-stage PV inverter with the parameters given in Table 4.3, the minimum allowed inverter input voltage is 294 V. The upper limit is limited based on the switches, and here chosen to be 1000 V. When the boost converter controls the PV voltage, the upper limit is defined by the dc-link voltage since the boost converter cannot increase its input voltage higher than the output voltage due to its structure as discussed in Chapter 2. In Fig. 4.16 is shown a step-test of the PV voltage along its achievable range in both single- and double-stage scenarios with the 120 V, 60 Hz system. In the double-stage PV inverter case, 2 PV modules are used, and in the single-stage, 8 PV modules.

In Fig. 4.17 is demonstrated how the PV voltage has distortion as the voltage increases close to the dc-link voltage (380 V) since the duty cycle is too close to 0. In Fig. 4.18 is demonstrated how the shape of the inverter ac-currents gets distorted at too low dc-side voltages due to overmodulation as discussed in Chapter 3.

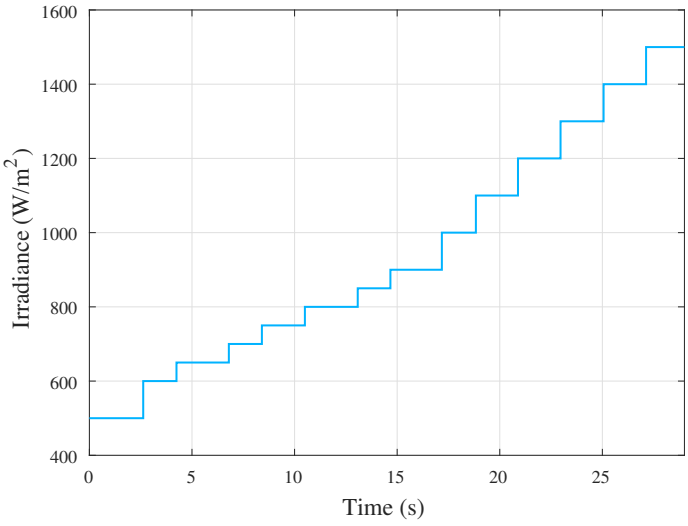

(a) Irradiance

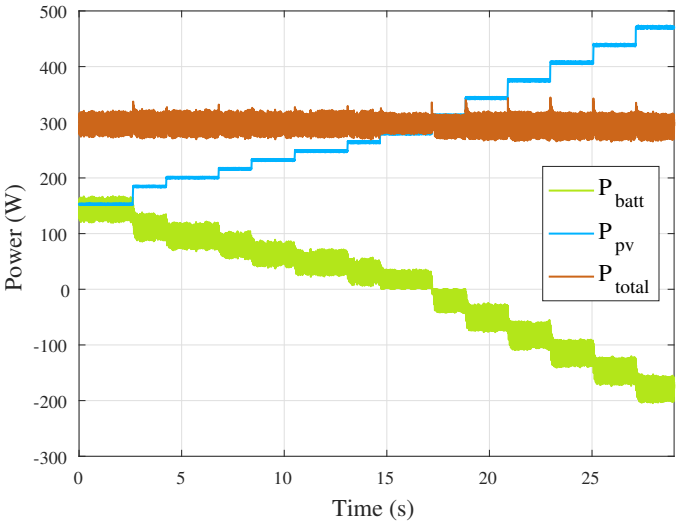

(b) The power produced by 2 PV modules, the compensating battery power, and the sum of these powers

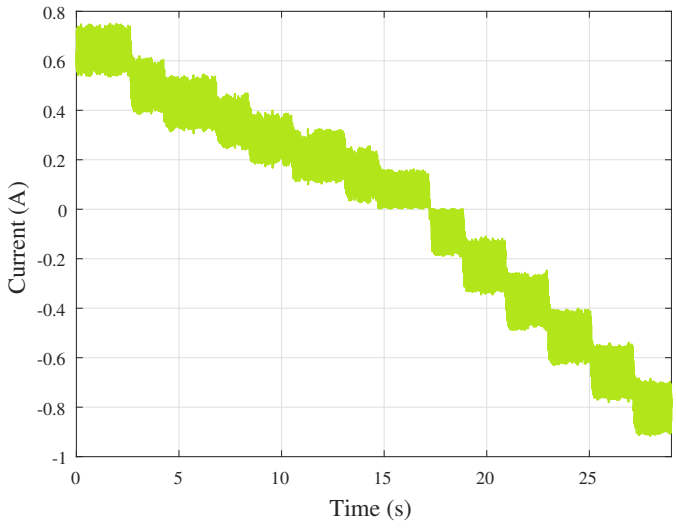

(c) Battery current

Figure 4.10 *Power balance control when the irradiance level is increased stepwisely as in (a) with the double-stage PV inverter topology using 2 PV modules. The grid power reference is set to 300 W*

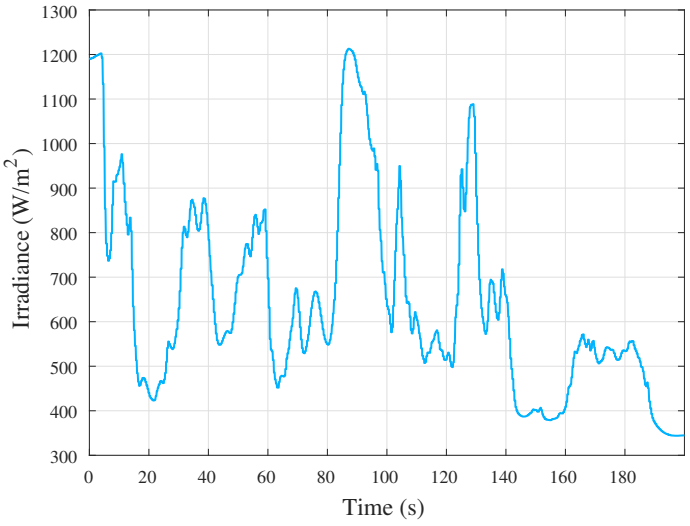

(a) Irradiance

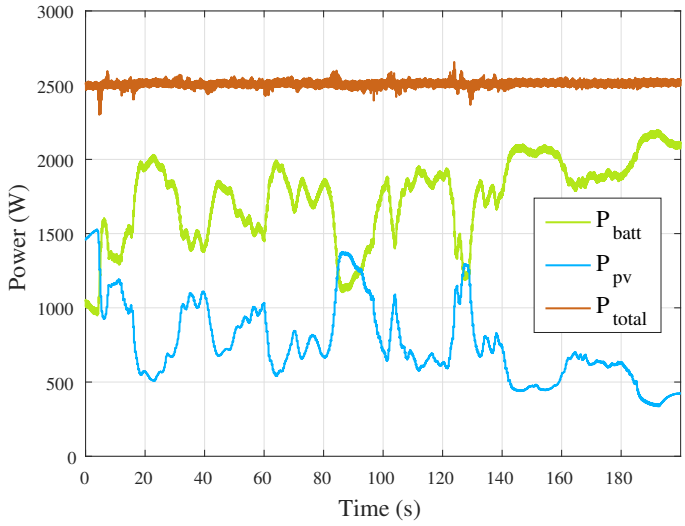

(b) The power produced by 8 PV modules, the compensating battery power, and the sum of these powers

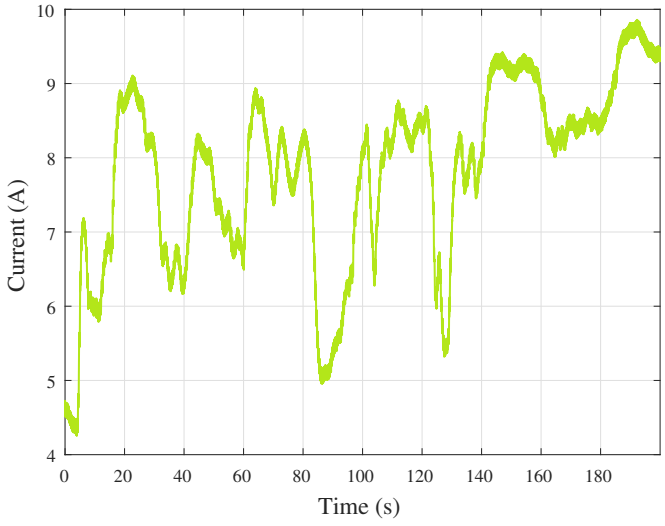

(c) Battery current

Figure 4.11 *Power balance control with the double-stage PV inverter topology using 8 PV modules. The grid power reference is set to 2550 W*

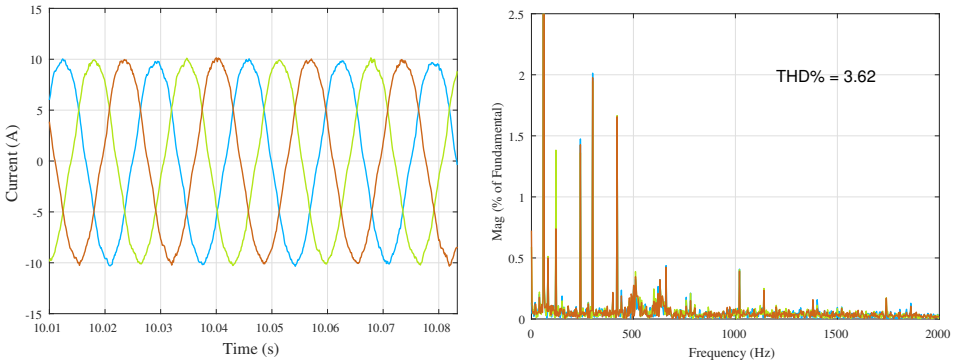

(a) Grid currents

(b) The harmonic spectrum of the grid current

Figure 4.12 *The grid currents and their harmonic spectrum corresponding to the operating points in Fig. 4.11*

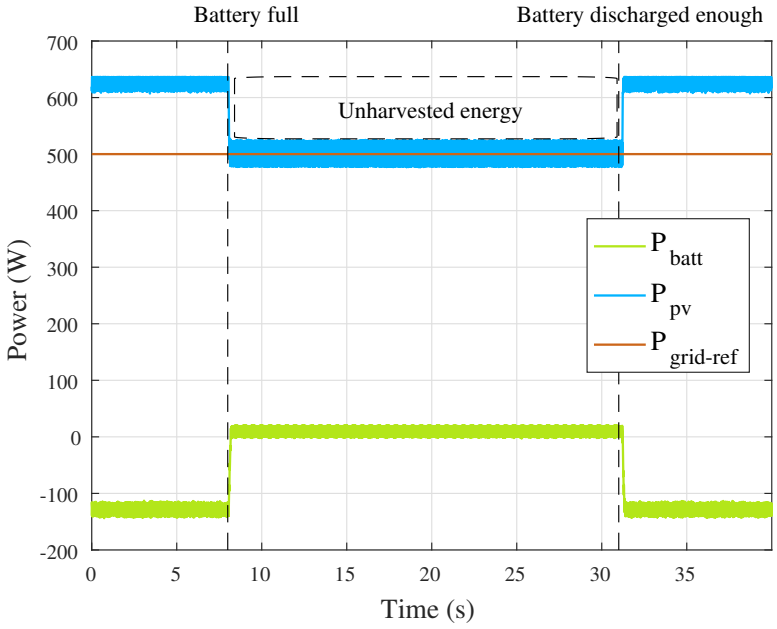

Figure 4.13 *An example of a situation, where the battery gets full so that MPPT cannot be used but a power limiting algorithm needs to be utilized instead until the battery has discharged enough and can be used again to store the excess power. The irradiance is kept constant*

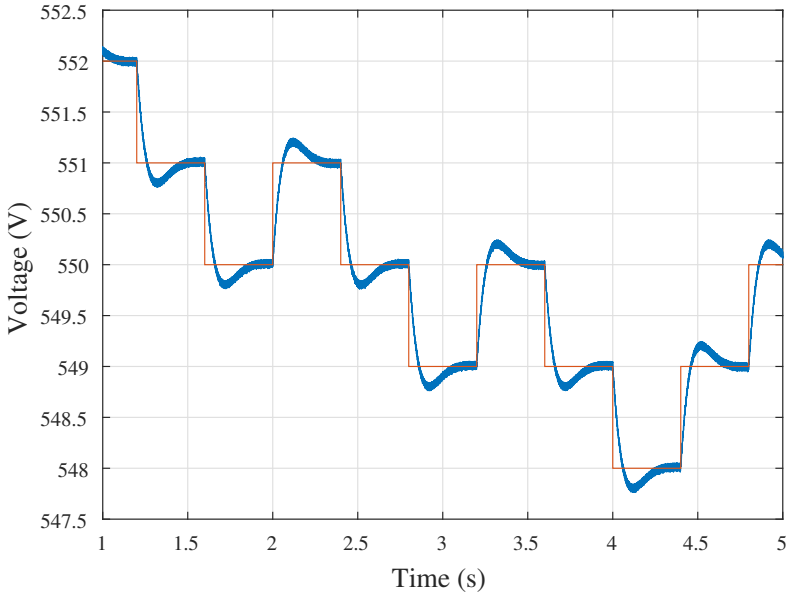

Figure 4.14 *PV voltage and reference controlled with the inverter with 5 Hz cross-over frequency*

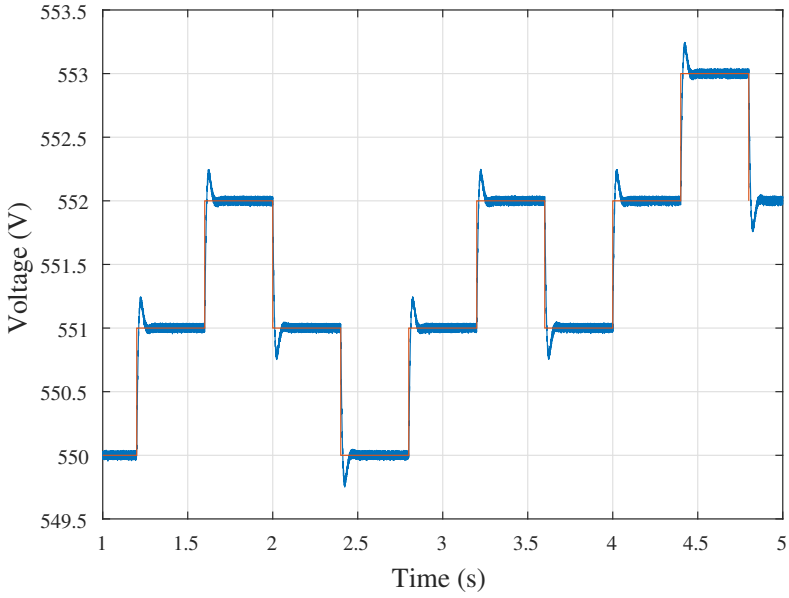

Figure 4.15 *PV voltage and reference controlled with the inverter with 25 Hz cross-over frequency*

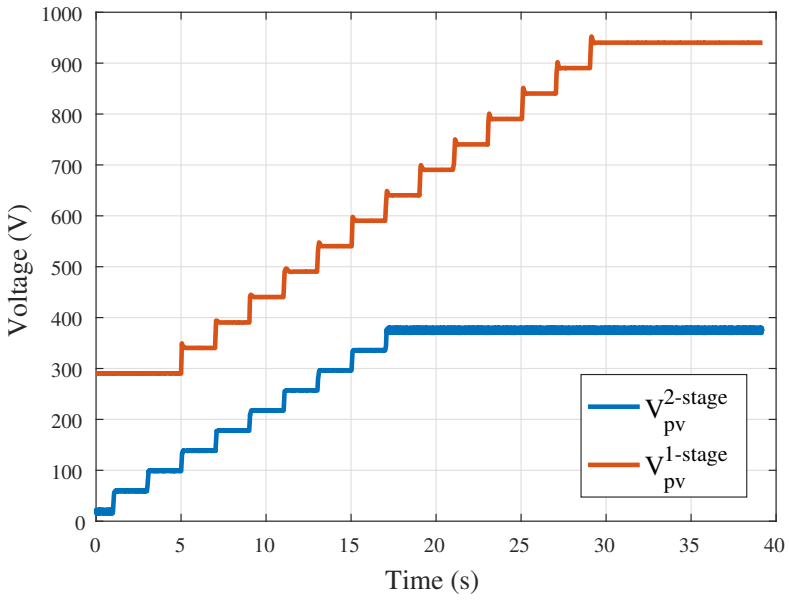

Figure 4.16 *Step-test of PV voltage along its range in both single- and double-stage scenarios with 120 V, 60 Hz three-phase system*

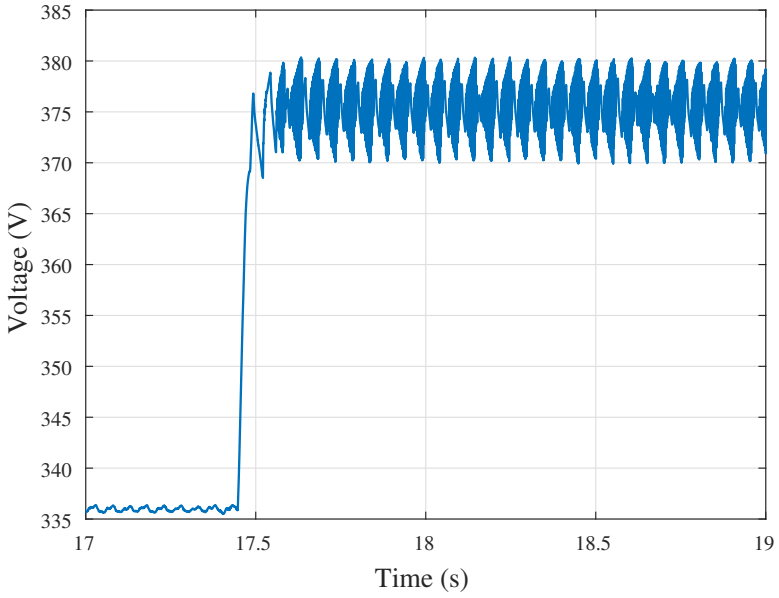

Figure 4.17 *The voltage across the PV modules controlled by the boost converter*

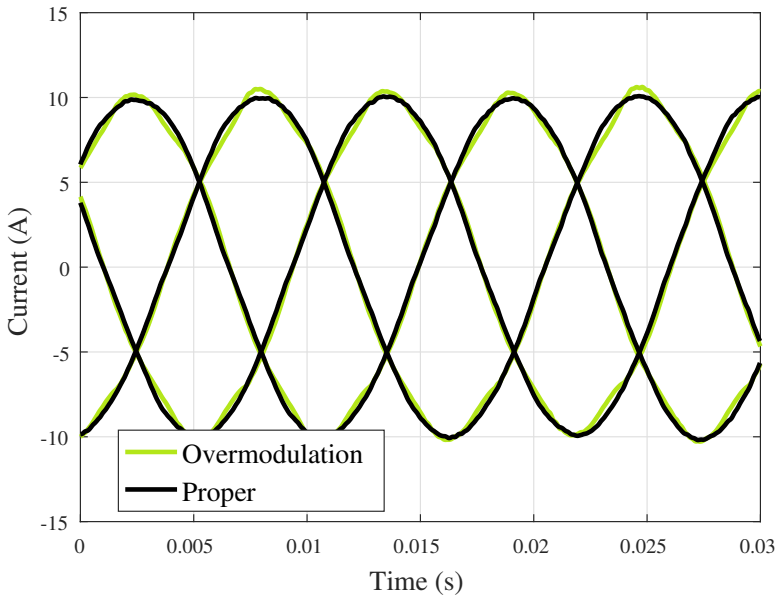

Figure 4.18 *The grid currents with and without overmodulation in a 60 Hz system*

5. CONCLUSIONS

The purpose of this thesis is to provide an insightful and meaningful comparison between the different power electronic topologies utilized in PV-EES DG systems. Numerous different topologies for this can be found in the literature. In order to narrow down the study, three different basic topologies are chosen for the comparison: single- and double-stage schemes and ac-interfaced batteries are investigated and compared. As discussed in Chapter 3, the choice of the most suitable topology is made on the basis of several variables and conditions. The chosen topologies are compared regarding part count, component sizing, reliability, efficiency, modularity, and control system complexity. The comparisons are conducted by analyzing the topologies and performing real-time simulator based studies.

A possible starting point for the decision of the topology is to find out, whether or not the control of the voltage across the PV modules can be achieved with the inverter or if an intermediate dc-dc converter is preferable. This decision defines, if the grid-connected electrical energy storage, such as a battery, can be attached to the same dc-link voltage or not. For instance, if the voltage across the PV modules at the highest temperature and lowest irradiation level under which it is supposed to be controlled is less than required by (3.1), the boosting dc-dc conversion stage is required. Note, that the same requirement applies to the batteries: The bi-directional dc-dc converter is necessary if the battery terminal voltage is lower than that required for the direct inverter connection. A battery system with high enough minimum voltage (and power) can be chosen, for example, the same way as presented in Fig. 3.5 for lithium-ion battery cells.

Since the dc-dc converter MPPT control of the PV voltage is specifically advantageous under partial shading conditions due to less PV modules required in series, the dc-dc converter is preferable for PV voltage control. This is assuming that the total amount of mismatch losses is greater than the losses caused by the additional conversion stage. Thus, in applications where partial shading conditions are typical, the dc-dc converter is preferable for PV voltage control. Nevertheless, in order to calculate the overall efficiency, the efficiency of the topology at each operating point and the amount of time spent at that operating point should be considered.

However, the inverter may be used to control the voltage across the PV modules instead of the dc-dc converter. Thus, the losses caused by the dc-dc converter are avoided and the topology is more efficient. The single-stage inverter is especially advantageous, if the MPPT speed and mismatch losses are not of concern. This is the case, for example, if the irradiance stays at high levels —even with fluctuation— since the variation of the MPP voltage at high irradiance is relatively smaller than at lower irradiance levels even when the irradiance varies (see Fig. 3.2 or Fig. 3.3). Although, as mentioned, it is important that the minimum voltage across the PV modules has to satisfy the requirement given in (3.1) to avoid overmodulation. Thus, multiple modules are required in series. Since mismatch losses etc. are not an issue for the battery current control, its control is more efficient with the single-stage inverter.

In addition, due to the cascaded control scheme of the inverter, where the dc-side voltage is controlled in the outer loop and the ac-side current d-component in the inner loop, the controller operates in a more effective way if the input voltage does not experience high fluctuation. This is not the case if the inverter is used for controlling the voltage across the PV modules instead of the dc-link voltage. As a result, the filtering requirements increase.

Finally, as demonstrated by performing real-time simulations with real irradiance data, the battery can be used for intermittency mitigation to compensate the fluctuations in the PV power (power balance), thus providing constant power to the grid. The converters used in the simulations were tuned based on their small-signal models utilizing loop-shaping technique.

BIBLIOGRAPHY

[1] G. Altintas, M. O. Gulbahce, and D. A. Kocabas, "Nonideal analysis, design and voltage mode control of a boost converter," in *2016 57th International Scientific Conference on Power and Electrical Engineering of Riga Technical University (RTUCON)*, Oct 2016, pp. 1–6.

[2] S. Armstrong, M. E. Glavin, and W. G. Hurley, "Comparison of battery charging algorithms for stand alone photovoltaic systems," *PESC Record - IEEE Annual Power Electronics Specialists Conference*, pp. 1469–1475, 2008.

[3] A. K. Barnes, J. C. Balda, and C. M. Stewart, "Selection of converter topologies for distributed energy resources," in *2012 Twenty-Seventh Annual IEEE Applied Power Electronics Conference and Exposition (APEC)*, Feb 2012, pp. 1418–1423.

[4] H. Beltran, E. Bilbao, E. Belenguer, I. Etxeberria-Otadui, and P. Rodriguez, "Evaluation of storage energy requirements for constant production in PV power plants," *IEEE Transactions on Industrial Electronics*, vol. 60, no. 3, pp. 1225–1234, 2013.

[5] F. Blaabjerg, Z. Chen, and S. B. Kjaer, "Power electronics as efficient interface in dispersed power generation systems," *IEEE Transactions on Power Electronics*, vol. 19, no. 5, pp. 1184–1194, Sept 2004.

[6] S. Buschhorn and K. Vogel, "Saving money: Sic in ups applications," in *PCIM Europe 2014; International Exhibition and Conference for Power Electronics, Intelligent Motion, Renewable Energy and Energy Management*, May 2014, pp. 1–7.

[7] M. Ceraolo, G. Lutzemberger, and D. Poli, "Aging evaluation of high power lithium cells subjected to micro-cycles," *Journal of Energy Storage*, vol. 6, pp. 116–124, 2016. [Online]. Available: http://dx.doi.org/10.1016/j.est.2016.03.006

[8] S. Dearborn, "Charging li-ion batteries for maximum run times," *Power Electronics Technology*, vol. 31, no. 4, pp. 40–49, 2005.

[9] Y. Ding, Y. Zhao, and G. Yu, "A membrane-free ferrocene-based high-rate semiliquid battery," *Nano Letters*, vol. 15, no. 6, pp. 4108–4113, 2015, pMID: 25942365. [Online]. Available: http://dx.doi.org/10.1021/acs.nanolett.5b01224

[10] R. Erickson and D. Maksimovic, *Fundamentals of Power Electronics*, ser. Power electronics. Springer US, 2001. [Online]. Available: https://books.google.fi/books?id=On9-rJTR8ygC

[11] V. Fthenakis and T. Nikolakakis, "Storage options for photovoltaics," in *Comprehensive Renewable Energy*, A. Sayigh, Ed. Oxford: Elsevier, 2012, pp. 199 – 212. [Online]. Available: http://www.sciencedirect.com/science/article/pii/B9780080878720001062

[12] W. Hhuijuan and Z. JianCheng, "Research on Charging/Discharging Control Strategy of Battery-Super Capacitor Hybrid Energy Storage System in Photovoltaic System," *2016 IEEE 8th International Power Electronics and Motion Control Conference*, no. 51177047, 2016.

[13] A. Q. Huang, "Power semiconductor devicesfor smart grid and renewable energy systems," *Proceedings of the IEEE*, vol. PP, no. 99, pp. 1–29, 2017.

[14] C. Jian, L. Yutian, and B. Guannan, "Optimal operating strategy for distribution networks with pv and bess considering flexible energy storage," in *2016 IEEE Power and Energy Society General Meeting (PESGM)*, July 2016, pp. 1–5.

[15] A. Jossen, J. Garche, and D. U. Sauer, "Operation conditions of batteries in PV applications," *Solar Energy*, vol. 76, no. 6, pp. 759–769, 2004.

[16] S. B. Kjaer, J. K. Pedersen, and F. Blaabjerg, "A review of single-phase grid-connected inverters for photovoltaic modules," *IEEE Transactions on Industry Applications*, vol. 41, no. 5, pp. 1292–1306, Sept 2005.

[17] S. Li, M. Fairbank, C. Johnson, D. C. Wunsch, E. Alonso, and J. L. Proao, "Artificial Neural Networks for Control of a Grid-Connected Rectifier/Inverter Under Disturbance, Dynamic and Power Converter Switching Conditions," *Neural Networks and Learning Systems, IEEE Transactions on*, vol. 25, no. 4, pp. 738–750, 2014.

[18] X. Li, D. Hui, and X. Lai, "Battery energy storage station (BESS)-based smoothing control of photovoltaic (PV) and wind power generation fluctuations," *IEEE Transactions on Sustainable Energy*, vol. 4, no. 2, pp. 464–473, 2013.

[19] M. Liserre, F. Blaabjerg, and S. Hansen, "Design and Control of an LCL - Filter-Based Three-Phase Active Rectifier," *IEEE Transactions on Industrial Applications*, vol. 41, no. 5, pp. 1281–1291, 2005.

[20] C. Liu, L. Lei, Q. Chen, L. Zhang, and S. Quan, "Model predictive control of single phase grid-connected inverter with lc filter," in *2017 32nd Youth Academic Annual Conference of Chinese Association of Automation (YAC)*, May 2017, pp. 115–119.

[21] Y. Liu, R. Bai, D. Wang, W. Ma, and L. Wang, "Proportional-resonant control method of three-phase grid-connected inverter," in *The 26th Chinese Control and Decision Conference (2014 CCDC)*, May 2014, pp. 4797–4800.

[22] Z. B. Mahmoud, M. Hamouda, and A. Khedher, "A comparative study of four widely-adopted mppt techniques for pv power systems," in *2016 4th International Conference on Control Engineering Information Technology (CEIT)*, Dec 2016, pp. 1–8.

[23] A. Mäki, "Effects of partial shading conditions on maximum power points and mismatch losses in silicon-based photovoltaic power generators," *Thesis*, 2013.

[24] T. Mesbahi, M. Meradji, G. Wang, D. Xu, and N. Rizoug, "Dynamic modeling and optimal control for series-parallel drivetrain based on lithium-ion battery," in *PCIM Europe 2016; International Exhibition and Conference for Power Electronics, Intelligent Motion, Renewable Energy and Energy Management*, May 2016, pp. 1–5.

[25] L. Nousiainen, J. Puukko, A. Mäki, T. Messo, J. Huusari, J. Jokipii, J. Viinamäki, D. T. Lobera, S. Valkealahti, and T. Suntio, "Photovoltaic generator as an input source for power electronic converters," *IEEE Transactions on Power Electronics*, vol. 28, no. 6, pp. 3028–3038, June 2013.

[26] K. Ogura, S. Chandhaket, S. Mekhilef, and M. Nakaoka, "New conceptual high efficiency sinewave pv power conditioner with partially-tracked dual mode step-up dc-dc converter," in *2015 IEEE 11th International Conference on Power Electronics and Drive Systems*, June 2015, pp. 847–854.

[27] A. Pirooz and R. Noroozian, "Model predictive control of classic bidirectional dc-dc converter for battery applications," in *2016 7th Power Electronics and Drive Systems Technologies Conference (PEDSTC)*, Feb 2016, pp. 517–522.

[28] S. Ponnaluri, G. O. Linhofer, J. K. Steinke, and P. K. Steimer, "Comparison of single and two stage topologies for interface of bess or fuel cell system using the abb standard power electronics building blocks," in *2005 European Conference on Power Electronics and Applications*, Sept 2005, pp. 9 pp.–P.9.

[29] J. Puukko, L. Nousiainen, A. Mäki, T. Messo, J. Huusari, and T. Suntio, "Photovoltaic generator as an input source for power electronic converters," in *2012 15th International Power Electronics and Motion Control Conference (EPE/PEMC)*, Sept 2012, pp. LS1d.2–1–LS1d.2–8.

[30] H. Qian, J. Zhang, J. S. Lai, and W. Yu, "A high-efficiency grid-tie battery energy storage system," *IEEE Transactions on Power Electronics*, vol. 26, no. 3, pp. 886–896, 2011.

[31] V. Rudolf and K. D. Papastergiou, "Financial analysis of utility scale photovoltaic plants with battery energy storage," *Energy Policy*, vol. 63, pp. 139–146, 2013. [Online]. Available: http://dx.doi.org/10.1016/j.enpol.2013.08.025

[32] U. Schwarzer, S. Buschhorn, and K. Vogel, "System benefits for solar inverters using sic semiconductor modules," in *PCIM Europe 2014; International Exhibition and Conference for Power Electronics, Intelligent Motion, Renewable Energy and Energy Management*, May 2014, pp. 1–8.

[33] M. E. V. Team. (2008) A guide to understanding battery specifications. [Online]. Available: http://web.mit.edu/evt/summary_battery_specifications.pdf

[34] O. Tremblay, L. A. Dessaint, and A. I. Dekkiche, "A generic battery model for the dynamic simulation of hybrid electric vehicles," in *2007 IEEE Vehicle Power and Propulsion Conference*, Sept 2007, pp. 284–289.

[35] A. Ulbig, T. S. Borsche, and G. Andersson, "Impact of low rotational inertia on power system stability and operation," 2014.

[36] J. Umuhoza, Y. Zhang, S. Zhao, and H. A. Mantooth, "An adaptive control strategy for power balance and the intermittency mitigation in battery-pv energy system at residential dc microgrid level," in *2017 IEEE Applied Power Electronics Conference and Exposition (APEC)*, March 2017, pp. 1341–1345.

[37] S. Vazquez, S. M. Lukic, E. Galvan, L. G. Franquelo, and J. M. Carrasco, "Energy storage systems for transport and grid applications," *IEEE Transactions on Industrial Electronics*, vol. 57, no. 12, pp. 3881–3895, Dec 2010.

[38] B. Wang, M. Zarghami, and M. Vaziri, "Energy management and peak-shaving in grid-connected photovoltaic systems integrated with battery storage," in *2016 North American Power Symposium (NAPS)*, Sept 2016, pp. 1–5.

[39] G. Wang, A. Q. Huang, F. Wang, X. Song, X. Ni, S. H. Ryu, D. Grider, M. Schupbach, and J. Palmour, "Static and dynamic performance characterization and comparison of 15 kv sic mosfet and 15 kv sic n-igbts," in *2015 IEEE 27th International Symposium on Power Semiconductor Devices IC's (ISPSD)*, May 2015, pp. 229–232.

[40] G. Wang, G. Konstantinou, C. D. Townsend, J. Pou, S. Vazquez, G. D. Demetriades, and V. G. Agelidis, "A review of power electronics for grid connection of utility-scale battery energy storage systems," *IEEE Transactions on Sustainable Energy*, vol. 7, no. 4, pp. 1778–1790, Oct 2016.

[41] T. C. Y. Wang, Z. Ye, G. Sinha, and X. Yuan, "Output filter design for a grid-interconnected three-phase inverter," in *Power Electronics Specialist Conference, 2003. PESC '03. 2003 IEEE 34th Annual*, vol. 2, June 2003, pp. 779–784 vol.2.

[42] S. Wenham, *Applied Photovoltaics*. Earthscan, 2007. [Online]. Available: https://books.google.fi/books?id=O3V-D5U3cWMC

[43] T. F. Wu, C. H. Chang, L. C. Lin, and C. L. Kuo, "Power loss comparison of single- and two-stage grid-connected photovoltaic systems," *IEEE Transactions on Energy Conversion*, vol. 26, no. 2, pp. 707–715, June 2011.

[44] W. Xiao, W. G. Dunford, P. R. Palmer, and A. Capel, "Regulation of photovoltaic voltage," *IEEE Transactions on Industrial Electronics*, vol. 54, no. 3, pp. 1365–1374, June 2007.

[45] K. Zhao, M. Pharr, J. J. Vlassak, and Z. Suo, "Fracture of electrodes in lithium-ion batteries caused by fast charging," *Journal of Applied Physics*, vol. 108, no. 7, p. 073517, 2010. [Online]. Available: http://dx.doi.org/10.1063/1.3492617

APPENDIX A. THE REAL-TIME SIMULATION SET-UP

The real-time simulations are conducted with the BoomBox control platform by Imperix, combined with the real-time emulator for hardware-in-the-loop (HIL) simulation by Typhoon-HIL.The set up consists of a Typhoon HIL 402, which is in charge of high-fidelity real-time simulation, interfaced with Imperix's Boombox, which is in charge of running the control code. A figure of the set-up is given below.

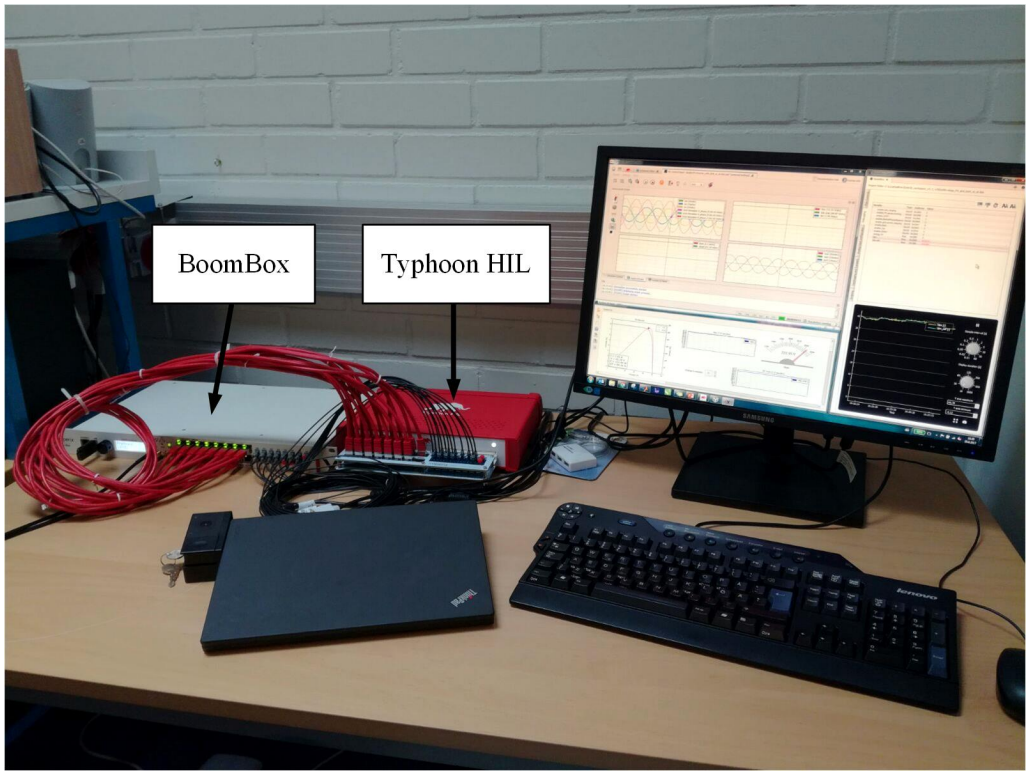

Figure 1 *The real-time simulation set-up*